



This is a repository copy of *Pore-network modelling of non-Darcy flow through heterogeneous porous media*.

White Rose Research Online URL for this paper:
<http://eprints.whiterose.ac.uk/148930/>

Version: Accepted Version

Article:

El-Zehairy, A.A., Nezhad, M.M., Joekar-Niasar, V. et al. (3 more authors) (2019)
Pore-network modelling of non-Darcy flow through heterogeneous porous media.
Advances in Water Resources, 131. 103378. ISSN 0309-1708

<https://doi.org/10.1016/j.advwatres.2019.103378>

Article available under the terms of the CC-BY-NC-ND licence
(<https://creativecommons.org/licenses/by-nc-nd/4.0/>).

Reuse

This article is distributed under the terms of the Creative Commons Attribution-NonCommercial-NoDerivs (CC BY-NC-ND) licence. This licence only allows you to download this work and share it with others as long as you credit the authors, but you can't change the article in any way or use it commercially. More information and the full terms of the licence here: <https://creativecommons.org/licenses/>

Takedown

If you consider content in White Rose Research Online to be in breach of UK law, please notify us by emailing eprints@whiterose.ac.uk including the URL of the record and the reason for the withdrawal request.



eprints@whiterose.ac.uk
<https://eprints.whiterose.ac.uk/>

Pore-network modelling of non-Darcy flow through heterogeneous porous media

A. A. El-Zehairy^{a,b,*}, M. Mousavi Nezhad^a, V. Joekar-Niasar^c, I. Guymet^d, N. Kourra^c, M. A. Williams^c

^a School of Engineering, Univ. of Warwick, Coventry CV4 7AL, U.K.

^b Irrigation & Hydraulic Engineering Dept., Faculty of Engineering, Mansoura Univ., Mansoura 35516, Egypt, el_zehairy@mans.edu.eg

^c School of Chemical Engineering and Analytical Science, University of Manchester, M13 9PL Manchester, UK

^d Department of Civil and Structural Engineering, University of Sheffield, Sheffield, UK

^e IMC, WMG, Univ. of Warwick, Coventry CV4 7AL, U.K.

*Corresponding author: E-mail: A.el-zehairy@warwick.ac.uk

Abstract

A pore-network model (PNM) was developed to simulate non-Darcy flow through porous media. This paper investigates the impact of micro-scale heterogeneity of porous media on the inertial flow using pore-network modelling based on micro X-ray Computed Tomography (XCT) data. Laboratory experiments were carried out on a packed glass spheres sample at flow rates from 0.001 to 0.1 l/s. A pore-network was extracted from the 3D XCT scanned volume of the 50 mm diameter sample to verify the reliability of the model. The validated model was used to evaluate the role of micro-heterogeneity in natural rocks samples. The model was also used to investigate the effect of pore heterogeneity on the onset of the non-Darcy flow regime, and to estimate values of the Darcy permeability, Forchheimer coefficient and apparent permeability of the porous media. The numerical results show that the Reynold's number at which nonlinear flow occurs, is up to several orders of magnitude smaller for the heterogeneous porous domain in comparison with that for the homogeneous porous media. For the Estailades carbonate rock sample, which has a high degree of heterogeneity, the resulting pressure distribution showed that the sample is composed of different zones, poorly connected to each other. The pressure values within each zone are nearly equal and this creates a number of stagnant zones within the sample and reduces the effective area for fluid flow. Consequently, the velocity distribution within the sample ranges from low, in stagnant zones, to high, at the connection between zones, where the inertial effects can be observed at a low pressure gradient.

33 **Keywords:** Non-Darcy Flow; Pore-network modelling; Forchheimer equation;
34 heterogeneous porous media.

35 **1. Introduction**

36 Many engineering transport phenomena are controlled by flow through porous media. To
37 reliably predict the flow, it is important to understand pore-scale factors and determine the
38 boundaries between different flow regimes. Neglecting the non-linear inertial effects according
39 to Stokes law, flow through porous media is usually modelled using Darcy's law (Equation 1)
40 (Darcy, 1856).

$$-\frac{\Delta P}{L} = \frac{\mu}{K_D} v \quad (1)$$

41 Darcy's law is a linear relationship between the pressure drop (ΔP) between two points
42 separated by distance (L) and the superficial or Darcy velocity ($v = \frac{q}{A}$), where q is the
43 volumetric fluid discharge, A is the whole cross-sectional area perpendicular to the flow
44 direction, μ is the fluid dynamic viscosity and K_D is the Darcy permeability. However, for
45 higher velocities, i.e. when the pressure drop due to inertial effects is $\geq 1\%$ of the total pressure
46 loss (Section 2.2.2), Equation 1 is no longer valid, and the inertial terms cannot be neglected.
47 Hence, the relationship between the pressure gradient and the superficial velocity becomes
48 non-linear.

49 In porous media, inertial effects can be expressed in the form of drag forces, and as was shown
50 by experiments, the pressure drop in such case is proportional to the summation of two terms;
51 one term includes the fluid velocity and represents the force exerted to overcome fluid
52 viscosity, whilst the other term includes the squared value of fluid velocity and represents the
53 force exerted to overcome fluid-medium interactions. The second term represents the inertial
54 effects which is a function of pore geometry, permeability and Reynold's number (Vafai &
55 Tien, 1981; Zeng & Grigg, 2006). Flow through the hyporheic zone, near groundwater wells,
56 or within hydraulic fractures in underground reservoirs are examples of flow in real
57 environment that show non-Darcy behaviour. For the non-Darcy flow regime, normally the
58 Forchheimer's equation is applied (Forchheimer, 1901). Forchheimer's equation (Equation 2)
59 is an extension to Darcy's law and was developed by adding a quadratic velocity term to
60 account for the non-linear inertial effects:

$$-\frac{\Delta P}{L} = \frac{\mu}{K_F} v + \rho \beta v^2 \quad (2)$$

61 where K_F is the Forchheimer permeability, that is very close to, but not the same as, Darcy
62 permeability (K_D), and ρ is the fluid density. β is the non-Darcy coefficient, also known as
63 Forchheimer coefficient, which is a medium dependent value similar to permeability. The non-
64 Darcy coefficient accounts for the inertial effects due to convergence, divergence and tortuosity
65 in the flow path geometry (Thauvin & Mohanty, 1998; Balhoff & Wheeler, 2009). Normally,
66 the β coefficient and the onset of non-Darcy flow regime are determined experimentally,
67 whereas some authors developed empirical relationships that predict β as a function of the
68 medium permeability, porosity and tortuosity (e.g. Thauvin and Mohanty (1998) and Liu et al.
69 (1995)).

70 To determine β and K_F from Forchheimer's equation, a linearized form of Equation 2 can be
71 used to determine the relation between $\frac{\Delta P}{L\mu v}$ or $\frac{1}{K_{app}}$, where K_{app} is the apparent permeability,
72 against $\frac{\rho v}{\mu}$. This should result in a straight line with slope β and intercept $1/K_F$ (Equation 3).

$$\frac{\Delta P}{L\mu v} = \frac{1}{K_{app}} = \frac{1}{K_F} + \beta \frac{\rho v}{\mu} \quad (3)$$

73 All experimental work has limitations, either due to difficulties or uncertainties in measuring
74 some quantities, mainly rooted from the complexity of the process. In such cases,
75 computational methods provide an alternative tool to gain insight into the processes. The
76 computational methods used for studying flow in porous media can be divided into
77 conventional continuum-scale numerical models and pore-scale models. Pore-scale models
78 have advantages over the continuum-scale numerical models as they provide details of the
79 physical process occurring at pore-scale, and their consequence at macroscale (Joekar-Niasar
80 & Hassanizadeh, 2012). Moreover, the medium parameters estimated from pore-scale studies
81 can be used to parameterize macro-scale equations (e.g. El-Zehairy et al., 2018).

82 To simulate single phase, incompressible, non-Darcy flow in a fully-saturated porous medium
83 at the macro-scale, typically the Navier-Stokes equations are used, simplified, averaged over
84 the simulation domains (fluid and solid phases), and then solved numerically. For example,
85 Zimmerman et al. (2004) and Zhang and Xing (2012) solved Navier-Stokes equations for
86 nonlinear flow using a finite-element mesh; Aly and Asai (2015) simulated non-Darcy flow
87 through porous media by the incompressible smooth particle hydrodynamics method and
88 Belhaj et al. (2003) used the Forchheimer equation to derive a finite difference model for Darcy
89 and non-Darcy flow in porous media. Many Computational Fluid Dynamics (CFD) software
90 packages such as ANSYS CFX, Fluent, and OpenFOAM solve these equations. However, there

91 are other models that can be used to simulate non-Darcy flow such as the Barree and Conway
92 model, the hydraulic radius model, A. V. Shenoy's Model, and the Fractal Model. Further
93 details about these models can be found in the review by Wu et al. (2016).

94 **1.1. Pore-scale modelling:**

95 Pore-scale models can be subdivided into six different groups: Lattice-Boltzmann (LB) models
96 (e.g., Kuwata and Suga, 2015), smoothed particle hydrodynamics (SPH) approach (e.g.,
97 Bandara et al. 2013), level-set models (e.g., Akhlaghi Amiri and Hamouda, 2013), percolation
98 models (e.g., Wilkinson, 1984), pore-network models (e.g., Bijeljic et al., 2004; Joekar-Niasar
99 et al. 2009) (Joekar-Niasar & Hassanizadeh, 2012) and direct numerical simulation (DNS)
100 (e.g., Raeini et al., 2012; Bijeljic et al., 2013b; Aziz et al., 2018). Percolation models cannot
101 reveal any transient processes information and all other methods are computationally more
102 expensive compared to pore-network models (Celia et al., 1995; Wang et al., 1999; Bijeljic et
103 al., 2004; Bijeljic & Blunt, 2007; Joekar-Niasar & Hassanizadeh, 2012; Blunt et al., 2013;
104 Oostrom et al., 2016). The SPH approach is a particle-based method, which although it has the
105 advantage of not being constrained by lattice points (e.g. similar to Lattice Boltzmann), it is
106 computationally more expensive (Tartakovsky et al., 2015). Dealing with a wide range of
107 contact angles in the level set method is challenging and significant efforts are spent on that.
108 DNS has been used mainly to simulate creeping flow through porous media, however, it could
109 also be used to simulate other flow regimes (e.g. Muljadi et al., 2015). Using DNS, the Navier-
110 Stokes equations are solved numerically on a mesh based on the voxelised X-ray Computed
111 Tomography (XCT) data of the medium. Using large mesh elements or large time steps will
112 lead to some errors at the small scales which will be transferred to the large scale and corrupt
113 the solution (Poinsot et al., 1995; Moin & Mahesh, 1998; Alfonsi, 2011; Mousavi Nezhad &
114 Javadi, 2011; Mousavi Nezhad et al., 2011).

115 In pore network modelling (PNM), the large pores constrained between the grains are referred
116 to as pore bodies (PB). The pore bodies are connected to each other by narrow paths which are
117 referred to as pore throats (PTh). Generally, the pore bodies are represented using spheres and
118 the pore throats are represented by cylinders or conical shapes. However, there are some studies
119 that considered other shapes for pore bodies and pore throats to enhance the accuracy of model
120 predictions (e.g. Joekar-Niasar et al., 2010). Connectivity is defined by the coordination
121 number which is the number of pore throats connected to a pore body. The PNM approach can
122 provide a simplified structure of complex porous media and allow the investigation of pore-

123 scale processes. It can also provide details of flow velocities and pressure fields for complex
124 heterogeneous pore spaces. Such information is essential to understand the flow behaviour and
125 for studying solute transport in heterogenous porous media.

126 Although many researchers have used pore-network modelling to investigate flow through
127 porous media, few have studied the flow within the laminar non-Darcy regime. The first study
128 was conducted by Thauvin and Mohanty (1998) and was limited to 3D regular lattice pore-
129 networks. To simulate the converging-diverging flow behaviour, Thauvin and Mohanty (1998)
130 used modified forms of two equations originally proposed by Bird et al. (1960) for modelling
131 pressure loss due to sudden expansion (diverging) and contraction (converging). Wang et al.
132 (1999) extended Thauvin and Mohanty's work for modelling non-Darcy flow through
133 anisotropic pore-networks, which was also limited to regular structured pore-networks. Later,
134 Lao et al. (2004) performed a study of non-Darcy flow using the Forchheimer equation
135 implemented in a two-dimensional random irregular pore-network with the maximum
136 coordination number of three. In another study, Lemley et al. (2007) used the Forchheimer
137 equation to simulate flow in a random unstructured three-dimensional (3D) pore-network, with
138 the upper limit of the coordination number in their network also three. The most recent study
139 for non-Darcy flow through 3D irregular unstructured pore-networks using the Forchheimer
140 equation is the work of Balhoff and Wheeler (2009). They argued that the equations presented
141 by Bird et al. (1960), are valid only for turbulent flow, despite the fact that these equations can
142 be derived from Bernoulli, continuity and momentum equations, so they are valid for all flow
143 conditions including laminar flow. Balhoff and Wheeler (2009) approximated the geometry of
144 pore throats by axisymmetric sinusoidal ducts and calculated the pressure loss through these
145 throats by solving the Navier-Stokes equations using a finite element method (FEM). After
146 doing the FEM simulations for pore throats with different dimensions, they provided a
147 relatively complex approximated equation that describes the pressure loss due to expansion
148 and contraction through each pore throat. Their equation depends on the flow rate and the pore
149 throat and the pore body geometries. However, their equation was developed for axisymmetric
150 ducts, and they defined the geometries of these ducts by a sinusoidal equation that implies the
151 pore bodies at the two ends of a pore throat to have an equal size, which is not likely to happen
152 in real porous media. None of these mentioned previous studies investigated the effect of pore
153 body and pore throat shape factors (G) on the flow simulation, which is considered of high
154 importance for natural porous media containing pores with irregular shapes. It is also necessary
155 for simulating two or multi-phase flow within the non-Darcy flow regime.

156 In porous media, heterogeneity can be expressed as the variation in shapes, sizes and
157 interconnectivity of the pores. Sahimi (2011) divided the heterogeneity of natural media into
158 four main categories; microscopic heterogeneities, macroscopic heterogeneities, field-scale
159 heterogeneities and gigascopic heterogeneities. Large-scale reservoirs can only be fully
160 determined if their measurable properties and features are detected at these different length
161 scales. With the help of modern imaging techniques, the internal morphologies of highly
162 complex material can be visualized and quantified in 3D. These geometric properties can be
163 detected at the resolution of few microns, with a field of view of a few millimetres (Knackstedt
164 et al., 2001).

165 In this paper, a 3D pore-network model was developed to simulate non-Darcy laminar flow
166 through porous media to address the impact of pore heterogeneity on the inertial flow and
167 hydraulic properties of the porous media. The model has been verified against experimental
168 data from packed glass spheres and some numerical results achieved through direct numerical
169 simulations. This work particularly focuses on the simulation of flow through natural porous
170 media using micro XCT 3D images. The effect of pore-scale flow processes (e.g. expansion
171 and contraction of flow) on macro-scale inertial flow behaviour has been investigated. It is
172 important to determine the velocity threshold above which the Darcy's law is not valid and a
173 non-Darcy model should be applied. Therefore, the model is applied to four porous media with
174 different structures and degrees of heterogeneity. The onset of a non-Darcy flow regime for
175 each sample has been determined, discussed and compared to previous research.

176 **2. Methodology**

177 **2.1. Pore-network extraction**

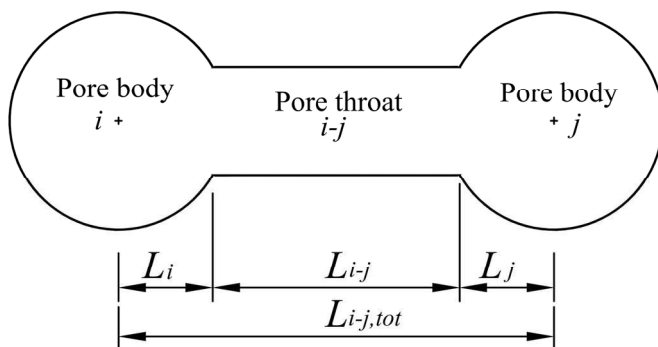
178 The reliability of predictions from pore-network modelling depends on firstly how accurately
179 the approximated pore-network represents the porous medium; and secondly, on the accuracy
180 of equations and the numerical schemes used for simulating the physical or chemical process
181 in the porous medium (Balhoff & Wheeler, 2009).

182 Pore-networks can be generated in three ways. The first approach is to extract the pore-network
183 directly from 3D images obtained using imaging technologies, such as XCT imaging, focused
184 ion beams, scanning electron microscopy and nuclear magnetic resonance (Xiong et al., 2016).
185 The second approach generates a representative pore-network using (geo)statistical
186 information such as pore body and pore throat size distributions, throat length distribution,
187 coordination number distribution and spatial correlation length (Al-Raoush et al., 2003; Gao et

188 al., 2012; Babaei & Joekar-Niasar, 2016). The third approach, the grain-based model, generates
 189 a pore-network based on the solid phase properties such as grain diameters and grain positions
 190 (Bryant & Blunt, 1992). This approach was further extended to generate pore-networks from
 191 grains affected by swelling, compaction or sedimentation (e.g. Bryant et al., 1993).
 192 In this study, for verification purposes, the first method is used to extract the pore-networks
 193 from four XCT 3D images: one packed glass spheres with average diameter (d_{avg}) = 1.84 mm,
 194 which is the same sample used in the experimental work, and the three other samples of
 195 beadpack, Bentheimer sandstone, and Estailades carbonate published in Muljadi et al. (2015)
 196 using the pore-network extraction code developed by Raeini et al. (2017). The pore-network
 197 extraction code can generate pore bodies and pore throats with triangular, square or circular
 198 cross-sections. The shape of the pore cross-sections is selected based on the level of irregularity
 199 over the wall of the narrow pores, which is quantified with shape factor, G . The shape factor is
 200 a dimensionless parameter, defined as $G = \frac{a}{p^2}$, where a is the average cross-sectional area of
 201 the pore throat or the pore body and p is the average perimeter (Mason & Morrow, 1991;
 202 Valvatne & Blunt, 2004). The value of the shape factor decreases when the shape of the surface
 203 of the pore space wall becomes irregular. According to geometrical definitions of 2D
 204 geometries, the value of shape factor ranges from zero, for a slit shape triangle, to $\frac{\sqrt{3}}{36}$ for
 205 equilateral triangle, whilst for squares and circles, the shape factor has values of $\frac{1}{16}$ and $\frac{1}{4\pi}$,
 206 respectively (Oren et al., 1998; Valvatne & Blunt, 2004). The shape factor definition for more
 207 complex geometries such as hyperbolic polygonal cross-sections can be found in Joekar-Niasar
 208 et al. (2010).

209 2.2. Mathematical modelling

210 2.2.1. Darcy flow modelling



211

212 **Fig. 1** Schematic of a pore throat ($i-j$) and two pore bodies (i and j).

213 In Darcy flow, the inertial effects are neglected and the flow rate (q_{i-j}) between two pore
 214 bodies i and j is given analytically by Hagen–Poiseuille equation (Hagen, 1839; Poiseuille,
 215 1841)

$$q_{i-j} = K_{i-j,tot} \Delta P_{i-j}^v = \frac{g_{i-j,tot}}{L_{i-j,tot}} \Delta P_{i-j}^v \quad (4)$$

216 Where $K_{i-j,tot} = \frac{g_{i-j,tot}}{L_{i-j,tot}}$, $g_{i-j,tot}$ is the fluid conductance, $L_{i-j,tot}$ is the length between the
 217 two pore body centres and ΔP_{i-j}^v represents the viscous pressure drop between the two pore
 218 bodies i and j . The conductance between the two pore bodies i and j is defined as harmonic
 219 mean of the conductances through the pore throat and the connected pore bodies (Oren et al.,
 220 1998; Valvatne & Blunt, 2004), given by

$$\frac{L_{i-j,tot}}{g_{i-j,tot}} = \frac{L_i}{g_i} + \frac{L_{i-j}}{g_{i-j}} + \frac{L_j}{g_j} \quad (5)$$

221 where $i-j$ indicates the connecting throat, L_{i-j} is the pore throat length excluding the lengths of
 222 the two connected pore bodies i and j , L_i and L_j are the pore body lengths from the pore throat
 223 interface to the pore centre (Fig. 1). For laminar flow in a circular tube the conductance g_{pore} is
 224 given analytically by the Hagen–Poiseuille equation (Hagen, 1839; Poiseuille, 1841)

$$g_{pore} = k \frac{a^2 G}{\mu} = \frac{1}{2} \frac{a^2 G}{\mu} \quad (6)$$

225 For equilateral triangular and square cross-sections, analytical expression can also be
 226 developed (Patzek & Silin, 2001; Valvatne & Blunt, 2004) with k equal to $3/5$ and 0.5623
 227 respectively. It has been also found that the conductance of irregular triangles can be
 228 approximated by equation (6), using the same constant ($k = 3/5$) as for an equilateral triangle
 229 (Oren et al., 1998; Valvatne & Blunt, 2004). The pore cross-sectional area (a) can be related
 230 to the shape factor as $a = \frac{r^2}{4G}$, where r is the radius of the inscribed circle inside the pore (Oren
 231 et al., 1998).

232 For each pore body i , considering incompressible steady flow, the mass conservation can be
 233 expressed as

$$\sum_{j \in N_i} q_{i-j} = 0 \quad (7)$$

234 where N_i is the coordination number of pore body i .

235 For the whole pore-network, Equation 4 is applied for each pore throat and Equation 7 is
 236 invoked at each pore body. In all simulations, no-flow boundary condition is applied for all
 237 pore-network boundaries except the inlet and outlet boundaries where constant pressure values
 238 are applied. This process results in a system of N linear equations, where N is the total number
 239 of pore bodies in the pore-network. Solving this system of equations using the method
 240 described in Babaei and Joekar-Niasar (2016), the pressure value at each node can be obtained
 241 and by applying Equation (4), the discharge through each pore throat can be estimated. Finally,
 242 the overall permeability (K_D) of the pore-network can be obtained by applying Darcy's law
 243 (Equation 1) for the whole pore-network.

244 In all simulations, the same fluid parameters used by Muljadi et al. (2015) are applied, water is
 245 considered as the working fluid with dynamic viscosity $\mu = 0.001$ kg/ms and density $\rho = 1000$
 246 kg/m³. The overall volumetric fluid discharge q is obtained by summing all pore throat
 247 discharges either at the inlet or the outlet of the pore-network, while the flow superficial
 248 velocity (v) is estimated as $v = \frac{q}{A}$. However, for highly heterogeneous media such as
 249 Estailades carbonate, the pore's cross-sectional area may differ significantly from one location
 250 to another, so using the whole cross-sectional area will cause uncertainties in q and K_D values.
 251 For that reason, for Estailades carbonate, the average pore velocity is estimated, then the
 252 superficial velocity (v) is derived as the average pore velocity times the medium porosity (ϕ).

253 2.2.2. Non-Darcy flow modelling

254 Following Muljadi et al. (2015) and Comiti et al. (2000), the onset of non-Darcy flow is
 255 assumed to be the point at which the pressure drop due to the linear term becomes less than
 256 99% of the total pressure drop. Using $\sqrt{K_D}$ to replace the characteristic length (L_{charc}) in the
 257 conventional Reynold's number (Re_L), so

$$258 \quad Re_L = \frac{\rho v L_{\text{charc}}}{\mu} \quad (8)$$

$$259 \quad Re_K = \frac{\rho v \sqrt{K_D}}{\mu} \quad (9)$$

260 where $\sqrt{K_D}$ is the Brinkman screening length (Durlafsky & Brady, 1987), i.e. the characteristic
 261 length is replaced by the square root of Darcy permeability to give the permeability based
 262 Reynold's number (Re_K).

261 For relatively high flow velocities, the inertial effects cannot be neglected as in the Darcy
 262 creeping flow regime. To consider the inertial effects due to expansion, when flow moves from

263 a pore throat to a connected pore body, and contraction, when flow moves from a pore body to
 264 a connected pore throat, the pressure loss due to these two processes should be considered in
 265 the calculation of total pressure drop through any pore throat. In the developed model, the
 266 pressure losses due to the inertial effects, expansion and contraction, are expressed using
 267 equations 10 and 11 (Kays, 1950; Abdelall et al., 2005; Guo et al., 2010; Momen et al., 2016).

$$\Delta P_{i-j}^{exp} = K_e \frac{\rho v_{i-j}^2}{2} = \left[\left(\frac{a_{i-j}}{a_j} \right)^2 (2 kd_j - \alpha_j) + \alpha_{i-j} - 2 kd_{i-j} \left(\frac{a_{i-j}}{a_j} \right) \right] \frac{\rho v_{i-j}^2}{2} \quad (10)$$

268 where ΔP_{i-j}^{exp} is the pressure loss due to expansion, K_e is the expansion coefficient, a_{i-j} and a_j
 269 are the cross-sectional areas of the pore throat and the connected pore body j , and v_{i-j} is the
 270 average fluid velocity through pore throat that connects the two pore bodies i and j . kd and α
 271 are the dimensionless momentum and kinetic-energy coefficients which depend on the velocity
 272 profile in each pore. For laminar flow, when the velocity is low and its profile is parabolic, kd
 273 is equal to 1.33, 1.39 and 1.43 for circular, square and equilateral triangular cross-sections
 274 respectively, while α is equal to 2 for circular cross-sections. For turbulent flow, when the
 275 velocity is high and its profile is almost uniform, kd and α are equal to ~ 1.0 (Kays, 1950).

$$\Delta P_{i-j}^{cont} = K_c \frac{\rho v_{i-j}^2}{2} = \left\{ \frac{1 - \left[\alpha_{i-j} \left(\frac{a_{i-j}}{a_j} \right)^2 - 2 kd_{i-j} + 1 - \left(\frac{a_{i-j}}{a_j} \right)^2 \right] Cc^2 - 2Cc}{Cc^2} \right\} \frac{\rho v_{i-j}^2}{2} \quad (11)$$

$$Cc = 1 - \frac{1 - \frac{a_{i-j}}{a_j}}{2.08 \left(1 - \frac{a_{i-j}}{a_j} \right) + 0.5371} \quad (12)$$

276 where ΔP_{i-j}^{cont} is the pressure loss due to contraction, K_c is the contraction coefficient, a_i is the
 277 cross-sectional area of the connected pore body i , Cc is the dimensionless jet contraction-area
 278 ratio (Vena-contraction) which can be estimated using Equation 12 (Geiger, 1964).

279 It has been found that using kd and α equal to 1.0 provides better representation of the non-
 280 Darcy flow which is characterised by higher velocities compared to the Darcy flow. This also
 281 agrees with the experimental findings of Abdelall et al. (2005) and Guo et al. (2010) performed
 282 on small channels. They showed that when using $kd = 1.33$ or $\alpha = 2.0$ in equations 10 and 11,
 283 this result in overestimation of K_e and K_c in most of the cases they tested. Moreover, when flow
 284 passes through a sudden expansion or contraction, this creates eddies and turbulence that make
 285 a flat velocity profile a better approximation for the flow. Using kd and α equal to 1.0, equations
 286 10 and 11 can be simplified and this results in the well-known Borda-Carnot equations (Crane,
 287 1942; Bird et al., 1961).

288 The total pressure loss for any pore throat in the network can be given according to Equation
 289 13 as follows:

$$\Delta P_{i-j}^{tot} = \Delta P_{i-j}^v + \Delta P_{i-j}^{exp} + \Delta P_{i-j}^{cont} = \left[\frac{L_{i-j,tot}}{g_{i-j,tot}} \right] q_{i-j} + K_e \frac{\rho q_{i-j}^2}{2a_{i-j}^2} + K_c \frac{\rho q_{i-j}^2}{2a_{i-j}^2}, \quad (13)$$

which can be written as

$$A_o q_{i-j}^2 + B_o q_{i-j} + C_o = 0.0 \quad (14)$$

290 where

$$291 \quad A_o = [K_e + K_c] \frac{\rho}{2a_{i-j}^2}, \quad B_o = \left[\frac{L_{i-j,tot}}{g_{i-j,tot}} \right], \quad C_o = -\Delta P_{i-j}^{tot}$$

292 To apply the continuity equation at each node, Equation 13 is rewritten in the form of a simple

293 quadratic equation (Equation 14), its positive root is equal to $q_{i-j} = \frac{-B_o + \sqrt{B_o^2 - 4A_o C_o}}{2A_o}$. For the

294 whole pore-network, Equation 13 is applied for each pore throat and Equation 7 is invoked at

295 each pore body. This process results in a system of N non-linear equations, where N is the total

296 number of pore bodies in the pore-network. A FORTRAN code was developed with the use of

297 HSL NS23 routine (HSL, 2013) to solve the resulting system of equations. The initial guess of

298 the pressure values at each node is provided from the Darcy flow case, then the HSL NS23

299 routine iterates until the final solution is achieved within an acceptable predefined error

300 criterion (until the sum of squares of residuals is less than 10^{-10}). By solving this nonlinear

301 system of equations, the pressure value at each node can be obtained and the discharge through

302 each pore throat is estimated by applying Equation 13. Finally, the non-Darcy coefficient (β)

303 and Forchheimer permeability (K_F) can be obtained by fitting a linear relationship to the

304 obtained results when $\frac{1}{K_{app}}$ is plotted against $\frac{\rho v}{\mu}$ (see Equation 3).

305 2.3. XCT-scanning and experimental work

306 To validate the proposed model, a porous medium sample (referred to as “packed spheres”)

307 composed of uniform spherical glass beads, with an average diameter (d_{avg}) of 1.84 ± 0.14 mm

308 was packed in a Perspex circular pipe of 300 mm length and 50 mm internal diameter. The

309 porous sample was placed in a recirculating pipe system with a sump of approximately 2.5 m^3 .

310 Water was used as a working fluid at different discharges ranging from 0.001 to 0.1 l/s. For

311 each run, the discharge was measured manually. The head loss measurements were performed

312 using two manometer tubes located 50 mm distance after the sample inlet and before the sample

313 outlet to eliminate the effect of boundaries on the flow, i.e. the head loss was measured through

314 a distance of 200 mm in the porous medium. To ensure the accuracy of manometric
315 measurements at low pressure gradients, an SPI digital depth gauge with accuracy ± 0.01 mm
316 was used to measure the manometric heads inside fixed, 25 mm wide manometric tubes.
317 Moreover, before taking any measurements, water was allowed to run through the recirculating
318 system for a period sufficient to remove any air from the system.

319 The middle part of the packed spheres sample used in the experimental work, which has the
320 dimensions of 50 mm \times 50 mm \times 177 mm, was scanned to determine the representative
321 elementary volume (REV) and to extract the equivalent pore-network. An REV can be defined
322 as a representative portion or subvolume of the medium, when selecting such volume at
323 different location in the sample, the resulting parameters (ϕ , K_D or β) of the subvolumes should
324 not vary significantly (Bear, 1972). To find an REV of the sample, a conventional approach
325 was followed, a code was written to generate random coordinates of cubic subvolumes with
326 different cube lengths (5, 10, 15, 20, 25, 30, 35 and 50 mm), and 10 different crops at random
327 locations have been tested for each cube size. For each single crop, a pore-network was
328 extracted, and the proposed pore-network model was used to estimate the porosity (ϕ), Darcy-
329 permeability (K_D) and non-Darcy coefficient (β), as in Section 3.3.

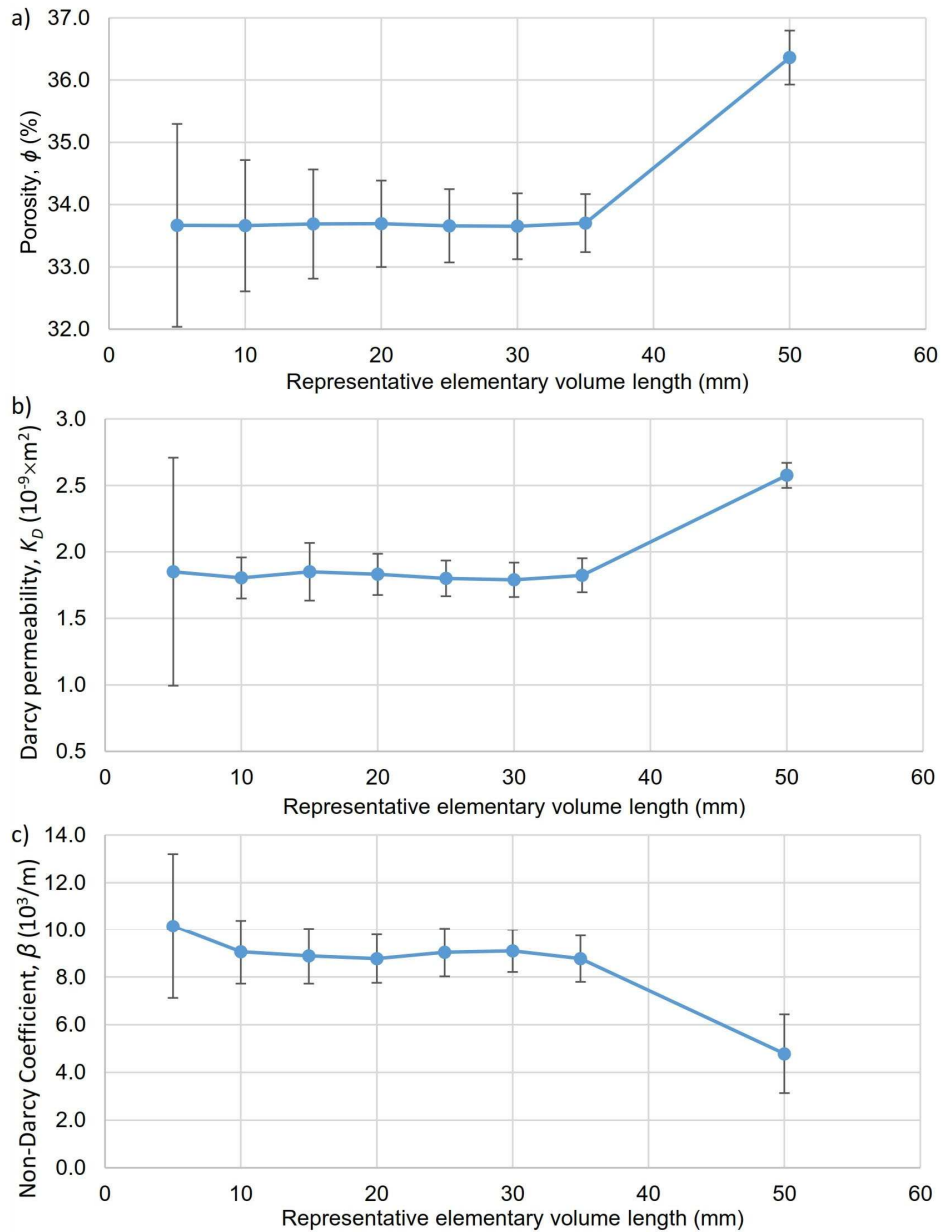
330 Four XCT scans were performed to examine the packed spheres sample utilising Nikon XT H
331 225/320 LC. The XCT settings were chosen to achieve optimum penetration and minimise
332 noise based on the grey values of the radiographs. A physical radiation filter of Tin (Sn) was
333 used to reduce beam hardening and cupping errors. The resolution of the scans was achieved
334 based on the diameter of the specimen. The scans were combined to provide the full volume of
335 the medium.

336 **3. Results and discussion**

337 **3.1. Determining the representative elementary volume (REV)**

338 Fig. 2 shows the effect of cube lengths on determining the porous medium properties. It can be
339 produced by applying the proposed model to the pore-networks extracted from all subvolume
340 crops of the packed spheres CT-image. In Fig. 2, it is observed that a suitable REV might be a
341 cube with length of 30 mm, which is a common value of the plateaus in figures 2a, 2b and 2c
342 associated with minimum fluctuation, i.e. minimum standard deviation. However, this is not
343 the case for the relatively small sample of 50 mm diameter used in the laboratory, considering
344 its large average bead diameter of 1.84 mm. For this specific case, using REV length less than
345 50 mm will result in eliminating the effect of the containing pipe wall or boundaries. Due to

346 the small size of the sample, the boundaries of the containing pipe have an effect on the
 347 estimated medium parameter as shown in Fig. 2. For that reason, an REV cube length of 50
 348 mm was selected to consider the effect of external pipe on the medium structure and on the
 349 flow behaviour through the medium.

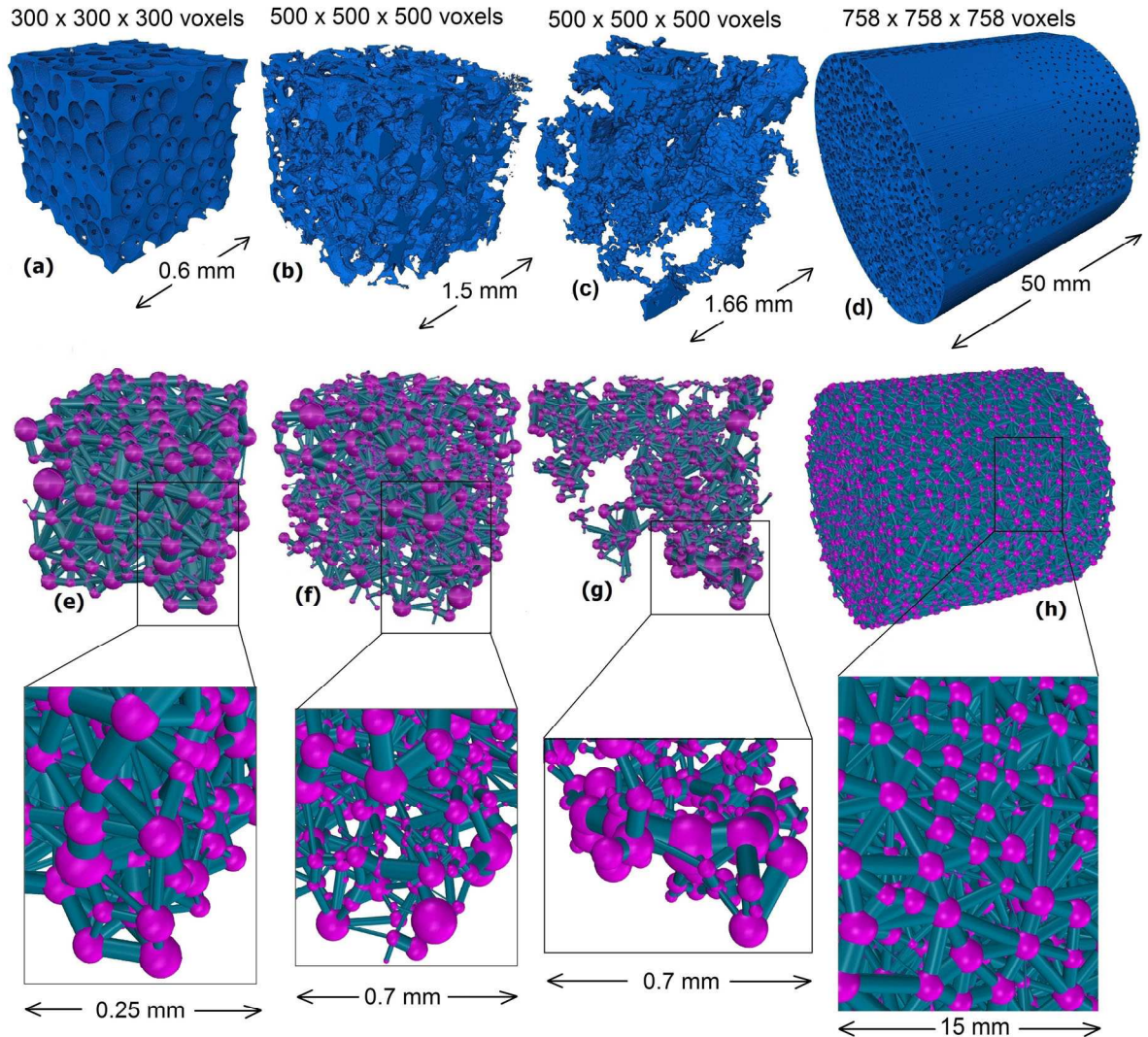


350
 351 **Fig. 2** Variation of a) porosity, b) Darcy-permeability and c) non-Darcy coefficient for different
 352 cubic subvolumes (10 crops for each REV length). The error bars represent the standard
 353 deviation of the estimated parameter for each REV length.

354

355 **3.2. Extracted pore-networks from CT-images**

356 Properties of the CT-images used to extract each of the four pore-networks shown in Fig. 3 are
357 provided in Table 1.



358

359 **Fig. 3** The pore spaces of (a) beadpack, (b) Bentheimer, (c) Estailades and (d) packed
360 spheres ($d_{avg} = 1.84$ mm), and the equivalent pore-networks (e), (f), (g) and (h) respectively.

361

362

363 **Table 1*:** The properties and characteristics length of the samples.

Sample	Resolution (μm)	Porosity, ϕ	Characteristic length, L_{charc} (μm)	Total voxels	Pore voxels	$K_D \times 10^{-12}$ (m^2) obtained by Muljadi et al. (2015) or in the experiments.
Beadpack	2.0	0.359	100	300×300×300	9,700,082	5.57
Bentheimer	3.0035	0.211	139.9	500×500×500	26,413,875	3.50
Estailades	3.3113	0.108	253.2	500×500×500	13,522,500	0.17
Packed spheres ($d_{\text{avg}} = 1.84$ mm)	65.99	0.364	1,837	758×758×758	124,612,700	2250

364 *For the first three samples, the characteristic length (L_{charc}) values are obtained from Muljadi et al. (2015); for
365 the unconsolidated beadpack they chose $L_{\text{charc}} = 100 \mu\text{m}$, while for consolidate porous media (Bentheimer and
366 Estailades) they followed the methodology in Mostaghimi et al. (2012) to determine L_{charc} as a function of the
367 specific surface area of the pore-grain interface (the surface area divided by the whole volume including pores
368 and grains). For the packed spheres ($d_{\text{avg}} = 1.84$ mm) sample, the characteristic length (L_{charc}) is the beads average
369 diameter (d_{avg}).

370

371 The 300×300×300 voxels beadpack image (Fig. 3a) represents a random packing of spheres of
372 uniform size. The image was created by Prodanović and Bryant (2006) to represent the
373 experimental measurements of the sphere centres obtained by Finney (1970). The only
374 available CT-image of Bentheimer sandstone sample used by Muljadi et al. (2015) is a
375 1000×1000×1000 voxels image. Unfortunately, the 500×500×500 voxels cropped image used
376 in their work is not available. Few trials were performed to crop that large image into a
377 500×500×500 voxels image at arbitrary locations, but this resulted in properties different to
378 those reported by Muljadi et al. (2015). To cope with that, the first 500 voxels in X, Y, and Z
379 directions of the large image (1000×1000×1000 voxels) were arbitrary cropped, then the pore-
380 network was extracted from that cropped image. This process will result in some uncertainties
381 with respect to the Bentheimer sandstone sample. The extracted pore-network properties of the
382 beadpack, Bentheimer sandstone, Estailades carbonate and REV of the packed spheres ($d_{\text{avg}} =$
383 1.84 mm) samples are shown in Table 2 and Fig. 3e-h. The histograms of inscribed pore body
384 and pore throat radii distributions for the four samples are shown in Fig.4.

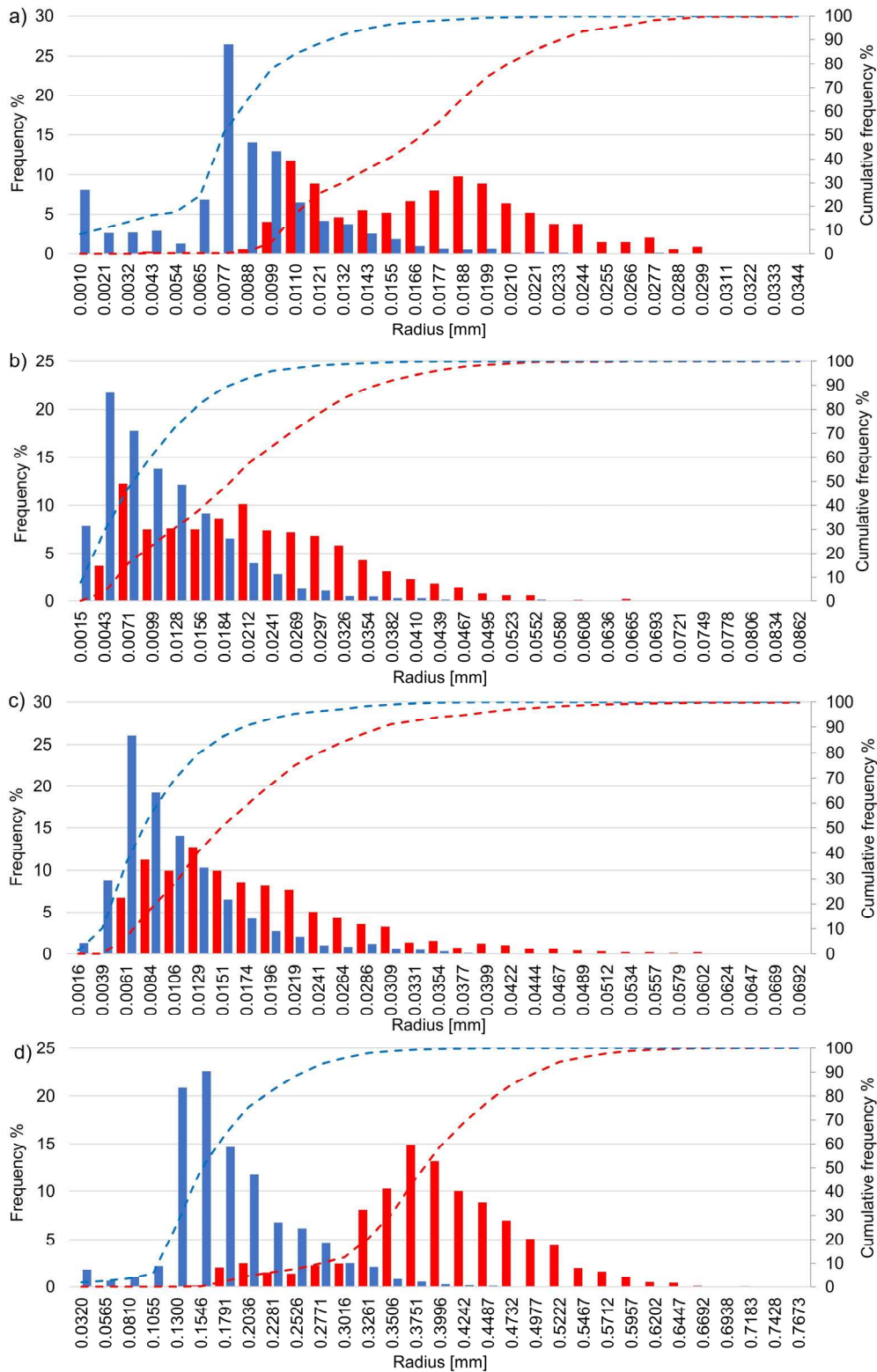
385 Investigations on pore-scale flow behaviour and the morphological characteristics of
386 Bentheimer sandstone and Estailades carbonate, have revealed that Estailades is more

387 heterogeneous than Bentheimer (Bijeljic et al., 2013a; Bijeljic et al., 2013b; Guadagnini et al.,
 388 2014; Muljadi et al., 2015). This was also confirmed by plotting the semi-variograms of pore
 389 body radii and coordination numbers of each sample (Figure S1 and S2 in supplementary
 390 materials).

391 **Table 2:** The properties of the extracted pore-networks.

Sample	Beadpack	Bentheimer (500×500×500 voxels)	Estailades	Packed spheres (d_{avg} = 1.84 mm)
Number of PBs	347	1033	954	10315
Number of PThs	1424	2418	1649	53960
Average coordination number	7.9	4.5	3.4	10.4
Maximum coordination number	21	23	19	30
Maximum inscribed PB radius (mm)	0.0344	0.0862	0.0692	0.7673
Average inscribed PB radius (mm)	0.0178	0.0231	0.0196	0.4103
Minimum inscribed PB radius (mm)	0.0051	0.0058	0.0064	0.1408
Maximum inscribed PTh radius (mm)	0.0287	0.0571	0.0575	0.6958
Average inscribed PTh radius (mm)	0.0089	0.0122	0.0116	0.1952
Minimum inscribed PTh radius (mm)	0.0009	0.0015	0.0016	0.0320

392



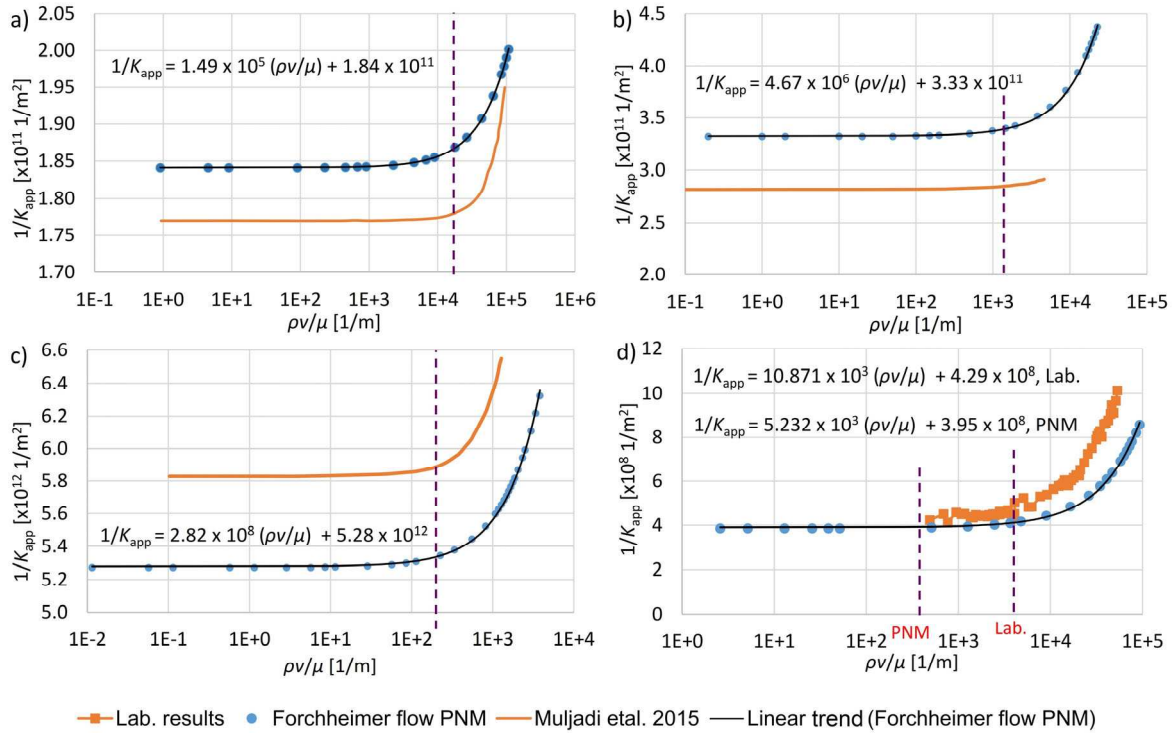
393

394 **Fig. 4** Histograms of inscribed pore body and pore throat radii for the four samples; a)
 395 beadpack, b) Bentheimer, c) Estailades and d) packed spheres.

396 3.3. Darcy permeability (K_D) and the non-Darcy coefficient (β)

397 The Darcy permeability (K_D) values obtained from PNM, by applying Darcy's law while
398 neglecting the inertial effects, are in a good match (varying less than 15.2%) with the
399 corresponding values in Muljadi et al. (2015) or obtained from experiments, as presented in
400 Table 3. Relatively large discrepancies (14% and 15.2%) are observed for Bentheimer and the
401 packed spheres ($d_{avg}=1.84$ mm) because the large Bentheimer image was cropped in an
402 arbitrary location and because the packed spheres sample was scanned prior to experiments, so
403 during experiments the position of some particles might have changed slightly under the effect
404 of flow at large velocities. Also, the pore-network extraction code defines the parameters of
405 pore-network elements using single phase direct numerical simulation on the CT-image, these
406 details can be found in Raeini et al. (2017) and Raeini et al. (2018). That is why the PNM
407 simulations can accurately reproduce the results predicted with direct simulation (by Muljadi
408 et al., 2015) and differ from the results achieved by experiments.

409 Fig. 5 shows a Forchheimer plot which is a plot of the inverse of apparent permeability $\left(\frac{1}{K_{app}}\right)$
410 versus $\left(\frac{\rho v}{\mu}\right)$. The slope of each graph represents the non-Darcy coefficient (β) and it is equal to
411 1.49×10^5 , 4.67×10^6 , 2.82×10^8 and 5.232×10^3 (1/m) for Beadpack, Bentheimer, Estailades and
412 packed spheres, respectively. The corresponding β values obtained from Muljadi et al. (2015)
413 and in the Laboratory are 2.57×10^5 , 2.07×10^6 , 6.15×10^8 and 10.87×10^3 (1/m), see Table 3. It
414 is noticeable that β values from PNM are in good match (within the same order of magnitude
415 and with maximum variation of 54%) with the values obtained by Muljadi et al. (2015) except
416 Bentheimer which has larger discrepancy (126%) because the cropped image used differs from
417 the image used by Muljadi et al. (2015). These discrepancies related to β values might be
418 because of the simplifications of pore shapes during the pore-network extraction. The shift in
419 the horizontal part of each curve when comparing PNM results to these by Muljadi et al. (2015),
420 or from experiments, are due to the difference in K_D obtained from different methodologies,
421 whilst the trend of each curve depends mainly on the pressure losses obtained at different
422 velocities.



424

425 **Fig. 5** Forchheimer plot for a) Beadpack, b) Bentheimer c) Estailades and d) experimental
 426 work vs. PNM. The vertical dashed lines represent the onset of non-Darcy flow.

427 **Table 3:** The permeability (K_D) and Forchheimer coefficient (β) for the four samples compared
 428 to those obtained by Muljadi et al. (2015) and by experiments.

Sample	Image voxels	total $K_D \times 10^{-12}$ (m^2), PNM	$K_D \times 10^{-12}$ (m^2) by Muljadi et al. (2015) or from Lab.	K_D difference [%]	$\beta \times 10^5$ (m^{-1}), PNM	$\beta \times 10^5$ (m^{-1}) by Muljadi et al. (2015) or from Lab.	β difference [%],
Beadpack	300×300×300	5.43	5.57	2.5	1.49	2.57	42
Bentheimer	500×500×500	3.01	3.50	14.0	46.7	20.7	126
Estailades	500×500×500	0.19	0.170	11.8	2820	6150	54
Packed spheres	758×758×758	2593	2250	15.2	0.0523	0.1087	52

429

430 3.4. Onset of non-Darcy flow

431 Fig. 6 shows the pressure gradient versus superficial velocity at different Reynold's numbers,
 432 the figure indicates also the onset of non-Darcy flow. The figure shows a good match with the
 433 previous results obtained by Muljadi et al. (2015) for Beadpack, Bentheimer and Estailades
 434 whilst there are larger discrepancies between PNM and laboratory results. A main cause of

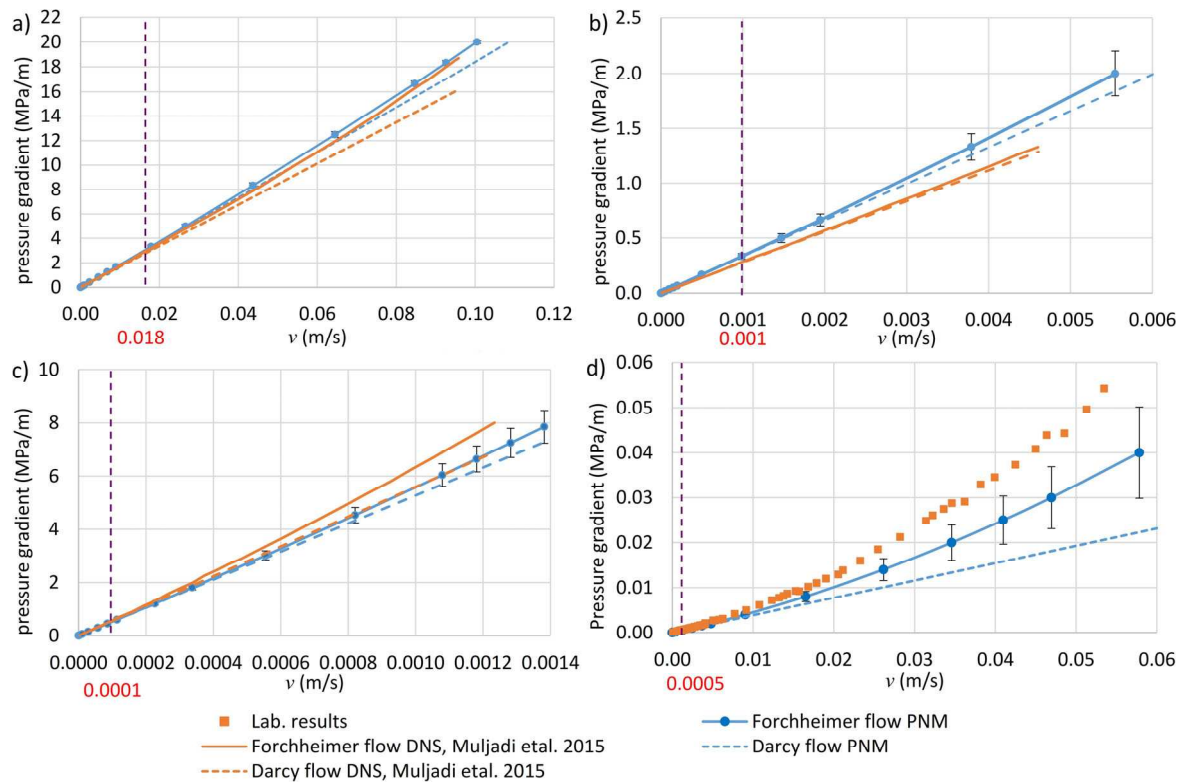
435 these larger discrepancies between PNM and laboratory is that the pores of the packed spheres
436 sample used in the experiments are significantly larger than the other three samples. When a
437 fluid enters a pore, its velocity profile is more likely to be uniform. The fluid then travels a
438 specific distance, known as the entrance length (L_h), until its velocity profile becomes fully
439 developed, i.e. parabolic velocity profile in case of pores with circular cross-section. In the
440 entrance length, the friction between the pore walls and the fluid is higher compared to fully
441 developed flow, and the Hagen–Poiseuille equation is not valid. For laminar flow, L_h is a
442 function of Reynold’s number and the pore diameter. It can be estimated as $L_h \cong 0.05 Re D_{pore}$
443 (Çengel & Cimbala, 2006), where Re is the pore Reynold’s number and D_{pore} is the pore
444 diameter which is considered as the characteristic length of the pore. For small pores, Re is low
445 and L_h is small and can be neglected compared to the total pore length. For that reason, the flow
446 in the majority of pores in the packed spheres sample is a developing flow, i.e. the pore
447 diameters are large and their lengths are not sufficiently long for a fully developed flow to be
448 achieved. This causes an underestimation of the friction factor of each pore in the sample if
449 Hagen–Poiseuille equation is used. This explains why the pressure losses obtained by PNM are
450 less than those obtained in the lab (Fig. 6d).

451 By estimating the average values of the entrance region (L_h) for all pore throats in the four
452 samples within the applied ranges of pressure gradients, it was found that L_h increases when
453 the applied pressure gradient increases. At the maximum applied pressure gradients, the
454 average values for L_h as a percentage of the average pore throats length were equal to 29%,
455 11% and 3% for the Beadpack, Bentheimer, and Estailades, respectively. For the packed
456 spheres sample, at the maximum applied pressure gradients, the average value of L_h , as a
457 percentage of the average pore throats length, reached 374%, which means that the pore lengths
458 are very short and even shorter than L_h . This demonstrates that the PNM approach has
459 limitations and the proposed set of equations cannot be applied for coarse media with large
460 pores.

461 Another possible reason for the discrepancy between the predicted results and those achieved
462 in the laboratory or through direct numerical simulations presented by Muljadi et al., (2015) is
463 the simplification that was implemented by PNM to describe the geometry of the samples.
464 Also, the mesh size used by Muljadi et al., (2015) may have effects on the accuracy of their
465 results.

466 According to the Forchheimer equation, the fluid velocity at any pressure gradient is a function
467 of two parameters (K_D and β) which are dependent on the geometry of the porous samples. The

468 superficial velocities calculated using the PNM at the onset of non-Darcy flow are 0.018, 0.001,
 469 0.0001 and 0.0005 m/s for Beadpack, Bentheimer, Estailades and packed spheres ($d_{avg} = 1.84$
 470 mm) sample respectively, while the corresponding values presented in Muljadi et al. (2015)
 471 and measured in the lab are 0.0279, 0.0014, 0.000227, and 0.004 m/s, see Table 4. It is
 472 noticeable that the onset of non-Darcy flow by PNM is in a good match with that obtained by
 473 Muljadi et al. (2015), but one order of magnitude lower than the values obtained from
 474 experimental measurements which is attributed to the large pore sizes for packed spheres
 475 sample and the large entrance length of its pores are explained earlier. In general, it is noticeable
 476 that the onset of non-Darcy flow occurs earlier, at lower velocities, when the medium has
 477 higher degree of heterogeneity. This is due to a reduction in the effective area for fluid flow in
 478 heterogeneous media, as shown in Section 3.5.



479
 480 **Fig. 6** The pressure gradient versus superficial velocity for both linear Darcy flow and
 481 nonlinear Forchheimer flow compared to the results by Muljadi et al. (2015) and laboratory
 482 measurements; a) is Beadpack, b) is Bentheimer, c) is Estailades and d) is the packed spheres
 483 sample. The error bars show the difference between the pressure gradient (at specific velocity
 484 values) for the Forchheimer flow case and the corresponding values obtained either by Muljadi
 485 et al. (2015) or via experimental measurements.

486 Considering the dimensionless apparent permeability (K^*) as

$$K^* = \frac{K_{app}}{K_D} \quad (15)$$

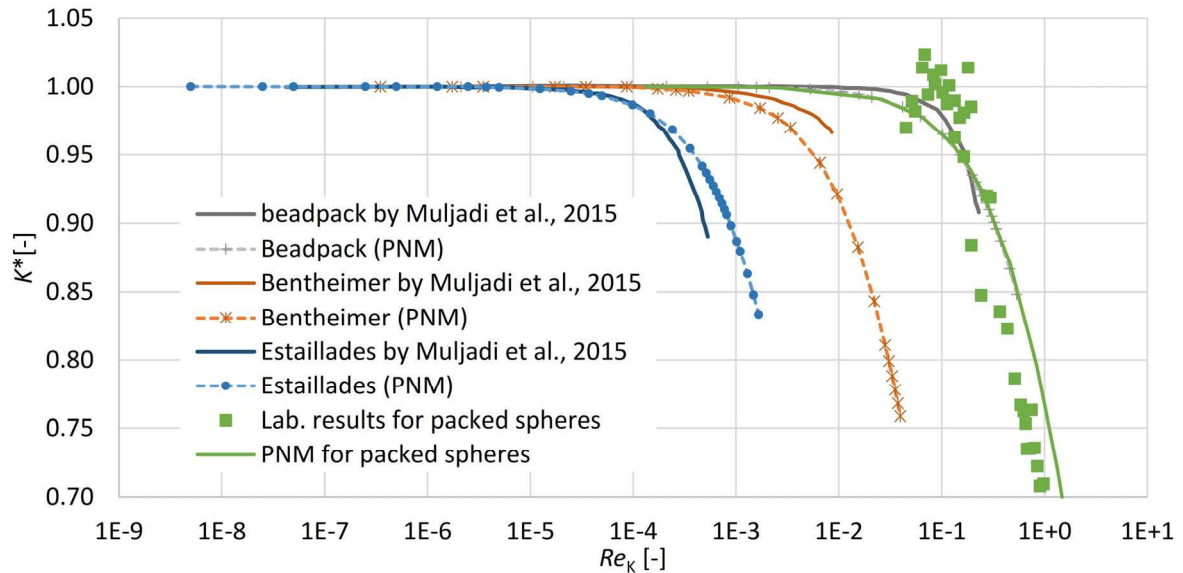
487 and following the same definition for the onset of non-Darcy flow in Section 2.2.2., from
 488 equations 1 and 3, the onset of non-Darcy flow can be determined when K^* is equal to 0.99 in
 489 Figs. 7 and 8. The predicted superficial velocities and Reynold's number values for the onset
 490 of non-Darcy flow and the corresponding values obtained either in Muljadi et al. (2015) work
 491 or in the laboratory are shown in Table 4.

492 In Fig. 7 and Fig. 8, the dimensionless apparent permeability (K^*) is plotted against Re_K and
 493 Re_L while using the same characteristic lengths (L_{charc}) used in Muljadi et al. (2015). PNM
 494 curves in Fig. 7 and Fig. 8 have similar trends to those in Muljadi et al. (2015) and in the
 495 laboratory, but a better match is obtained, especially for Estailades, in Fig. 7 when Re_K is used
 496 instead of Re_L . According to equations 3, 8, 9 and 15 this mismatch is attributed either to the
 497 change in superficial velocities or pressure losses in both studies. Therefore, these
 498 discrepancies are attributed to the difference between PNM Darcy flow and Forchheimer flow
 499 curves in Fig. 6 compared to the difference between the two curves in Muljadi et al. (2015) or
 500 in the experimental results. Fig. 7 and Fig. 8 also confirm that the onset of non-Darcy flow
 501 occurs earlier, at low Reynold's number, in highly heterogenous media as in the case of
 502 Estailades carbonate. After determining the non-Darcy coefficients (β) for each sample (as
 503 shown in Section 3.3), and when the dimensionless apparent permeability (K^*) is plotted versus
 504 Forchheimer number ($F_o = \frac{K_D \beta \rho V}{\mu}$) in Fig. 9, the curves of all the samples coincide. This
 505 unique relationship can be derived mathematically from the Forchheimer Equation (Ruth &
 506 Ma, 1992; Ruth & Ma, 1993). In petrophysics, the relationship shown in Fig. 9 can be used to
 507 predict the apparent permeability for media with known K_D and β , without the need to perform
 508 laboratory experiments at different flow rates. K_D and β can be determined using literature data
 509 or empirical relationships such as those proposed by Kozeny (1927), Carman (1937), Ergun
 510 (1952), and Janicek and Katz (1955). In Fig. 9, the onset of non-Darcy flow occurs when $K^* =$
 511 0.99, and this corresponds to $F_o \approx 0.01$ for all PNM simulations and $F_o = 0.1$ for experimental
 512 results. These F_o values are in agreement with the range (0.01-0.1) proposed by Andrade et al.
 513 (1999).

514 It is importance to take into consideration the non-Darcy coefficient (β) when determining the
 515 onset on non-Darcy flow for different media. For that reason, in Fig. 10, the pressure gradient
 516 is plotted versus Forchheimer number, as this is a better comparison tool for follow up studies.
 517 The resulting plots are straight lines as expected according to Forchheimer equation (Equation

518 2). The onset of non-Darcy flow shown in the figure is determined using the superficial velocity
 519 at $K^* = 0.99$.

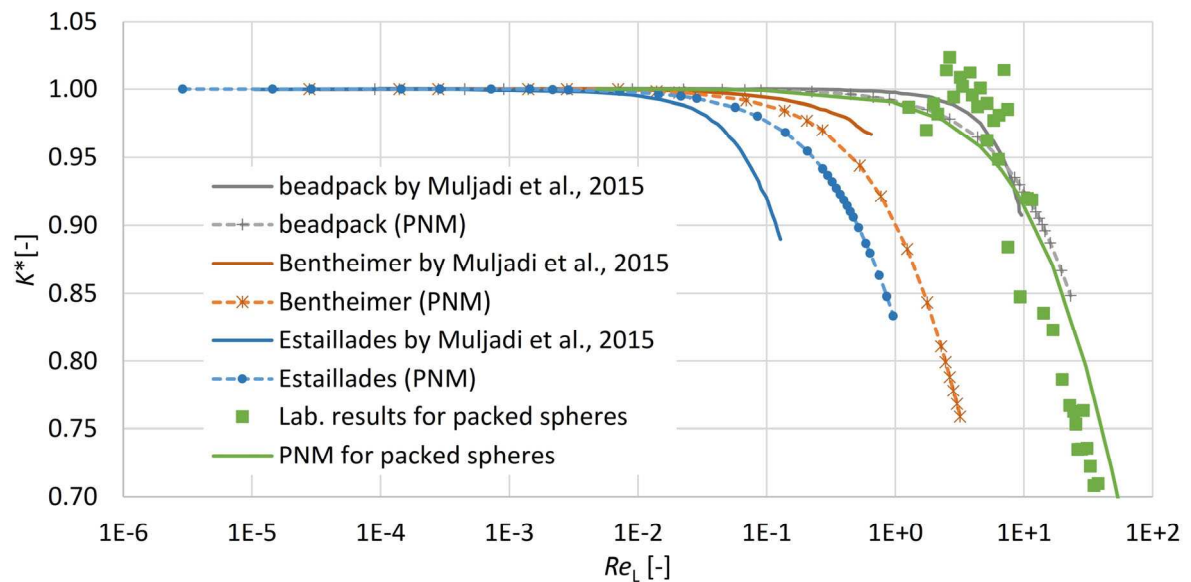
520



521

522 **Fig. 7** The dimensionless permeability K^* versus Re_K (Equation 9), compared to the results
 523 from Muljadi et al. (2015) and experiments.

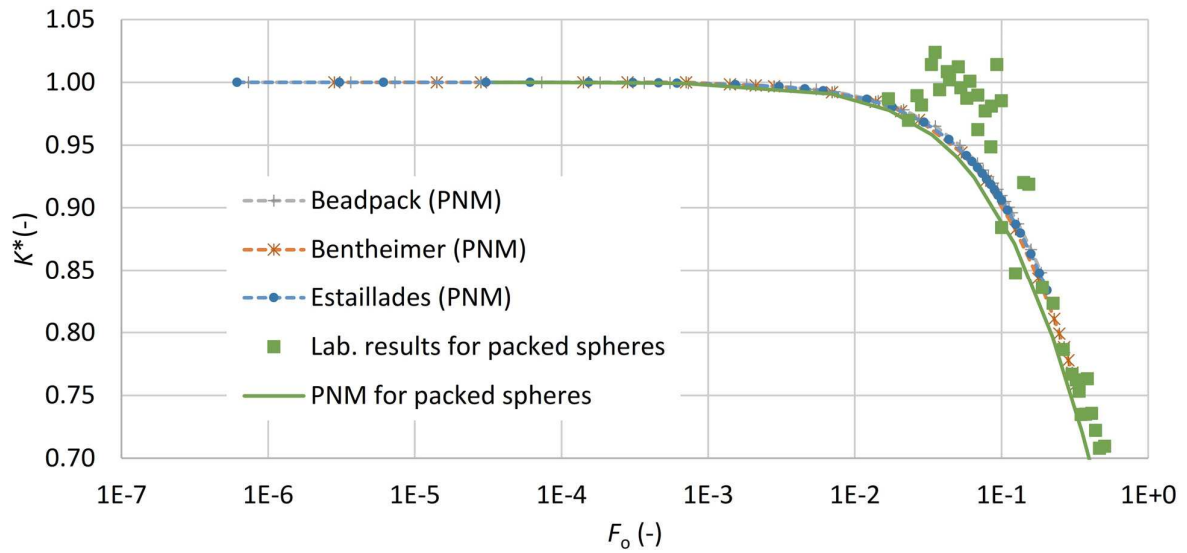
524



525

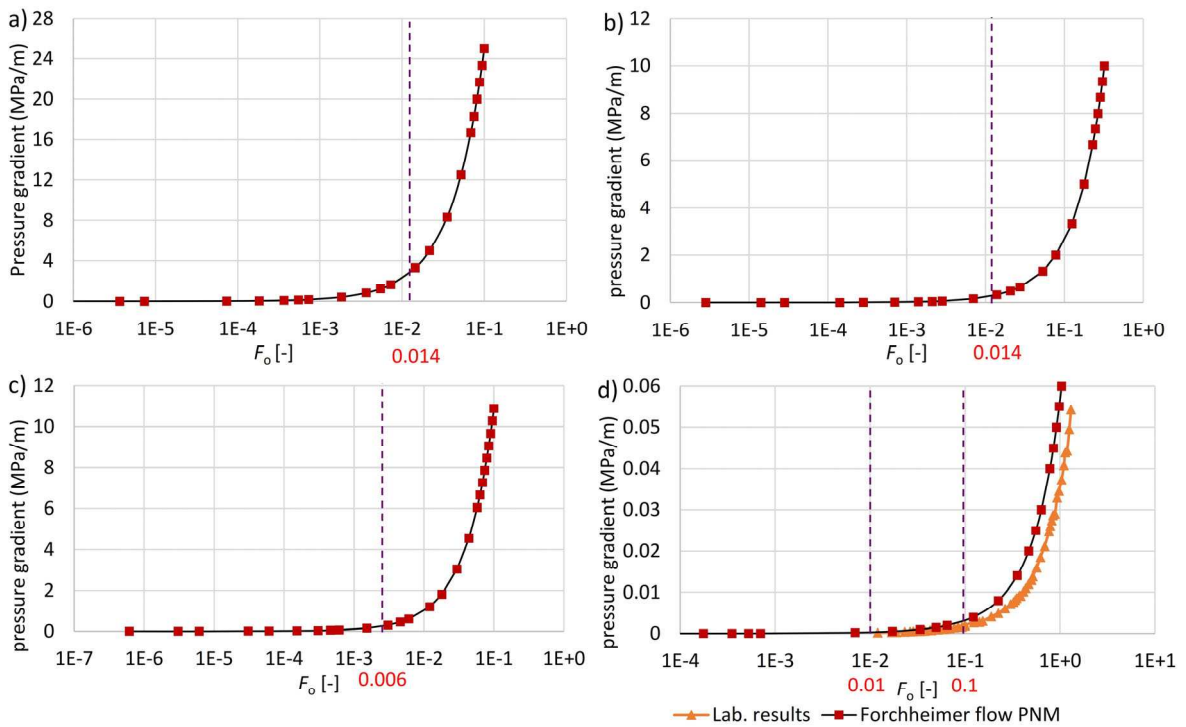
526 **Fig. 8** The dimensionless permeability K^* versus Re_L (Equation 8), compared to the results
 527 from Muljadi et al. (2015) and experiments.

528



529

530 **Fig. 9** The dimensionless permeability K^* versus F_o , compared to the results from
 531 experiments.



532

533 **Fig. 10** The pressure gradient versus Forchheimer number (F_o); a) Beadpack, b) Bentheimer c)
 534 Estailades and d) glass-bead packing experiments vs. pore-network modelling results.

535

536 **Table 4:** Reynold’s number and superficial velocity values for the onset of non-Darcy flow.

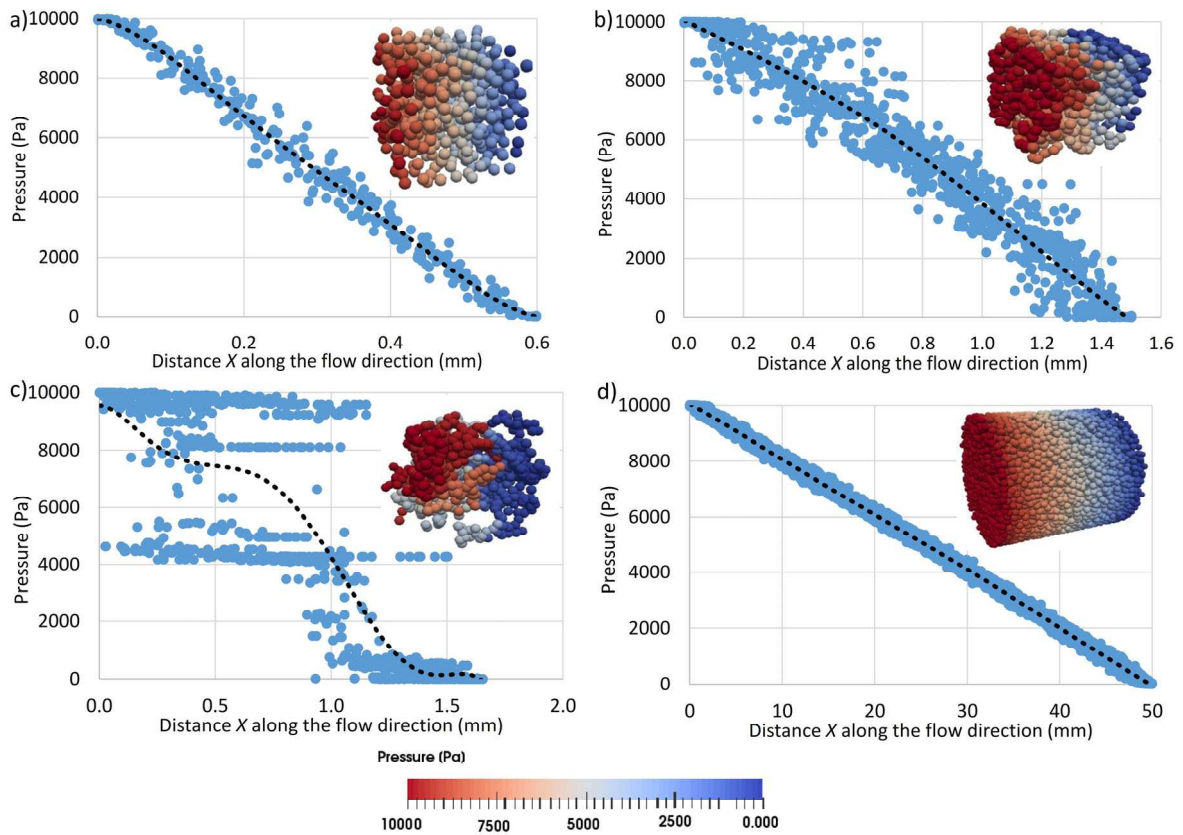
Sample	Onset of non-Darcy flow (pore-network modelling)			Onset of non-Darcy flow obtained by Muljadi et al. (2015) or in the experiments.			Difference [%],		
	v (mm/s)	Re_K	Re_L	v (mm/s)	Re_K	Re_L	v (mm/s)	Re_K	Re_L
Beadpack	17.83	4.15×10^{-2}	1.78	27.9	6.64×10^{-2}	2.79	36	38	36
Bentheimer	0.99	1.72×10^{-3}	0.14	1.4	2.64×10^{-3}	0.196	29	3	29
Estailades	0.11	4.79×10^{-5}	0.028	0.227	9.4×10^{-5}	0.023	52	5	22
Packed spheres ($d_{avg}=1.84$ mm)	0.51	2.60×10^{-2}	0.94	4.09	1.94×10^{-1}	7.54	88	87	88

537

538 **3.5. Effect of heterogeneity on Pressure distribution**

539 One of the advantages of the pore-network modelling approach is that it provides a detailed
540 overview of the pressure field at the pore-scale as presented in Fig. 11. Fig. 11 shows the
541 pressure value at each pore body versus distance (X) along the flow direction when applying
542 10000 Pascal pressure drop. The 3D pressure distribution at each pore body is shown at the top
543 right corner for each sub-figure. The dotted black curve represents the average pressure value
544 at any cross-section perpendicular on the flow direction. Inspection of Fig. 11 shows that for
545 the media with low degree of heterogeneity, i.e. beadpack, Bentheimer and packed spheres,
546 there is a regular change of pressure over distance. At any vertical cross-section perpendicular
547 to the flow direction, the maximum pressure variation between pores remains within 25% of
548 the overall pressure drop in the case of beadpack, 10% in the packed spheres and 45% in the
549 Bentheimer. Nevertheless, for highly heterogeneous media, Estailades, the pressure variation

550 between pores at one cross-section may extend up to 98% of the overall pressure drop. This is
 551 mainly caused by the medium heterogeneity that creates some stagnant zones with low pressure
 552 values next to the zones with high pressure. The pressure distribution in Fig. 11c shows that
 553 the sample is composed of several zones, poorly connected to each other. Therefore, the
 554 pressure values within each zone are nearly equal and are significantly different from the
 555 pressure values of other zones. Consequently, the velocity distribution within the sample ranges
 556 from low in stagnant zones to high at the connection between zones where the inertial effects
 557 can be observed even at low pressure gradients.



558

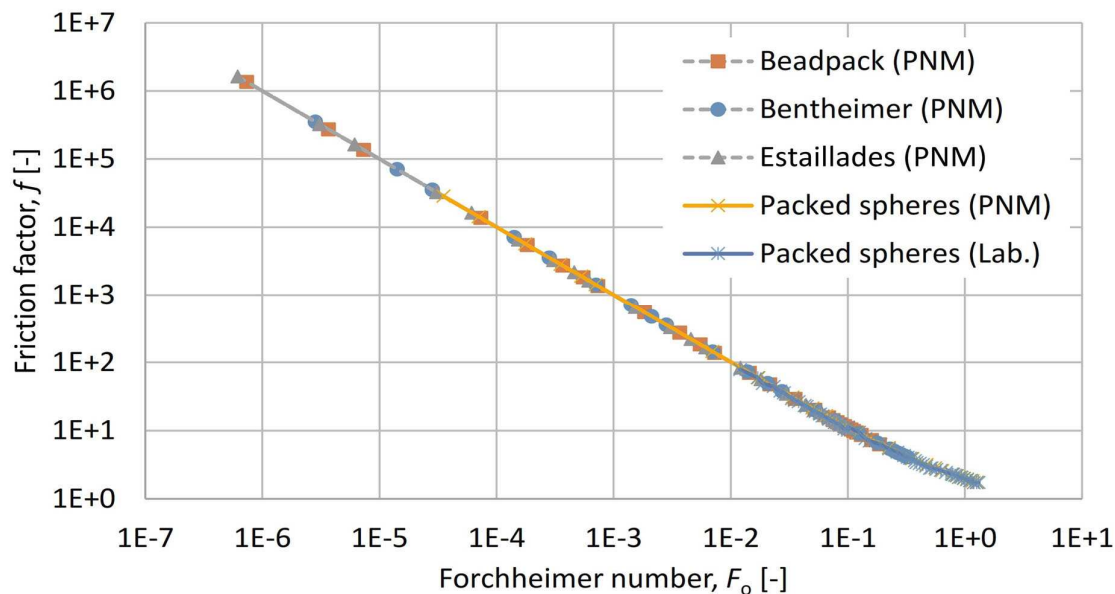
559 **Fig. 11** Pressure values at each pore body vs. distance (X) along the flow direction when
 560 applying 10000 Pascal pressure drop; a) Beadpack, b) Bentheimer, c) Estailledes and d) Packed
 561 spheres. The 3D pressure distribution at each pore body is shown at the top right corner of each
 562 sub-figure. The dotted black curve represents the average pressure value at any cross-section
 563 perpendicular on the flow direction. The flow direction is from left to right.

564 3.6. Friction factor

565 Similar to Hagen–Poiseuille equation (Hagen, 1839; Poiseuille, 1841) for laminar flow through
 566 pipes, Moody chart (Moody, 1944) is the most widely used chart for designing flow through
 567 pipes in all flow regimes. It is used to estimate the dimensionless friction factor (f) of a pipe at

568 specific Reynold's number, and from this friction factor, the pressure needed to pass the flow
 569 at specific rate through the pipe can be determined. Thinking of porous media as a group of
 570 connected pipes, (Carman, 1937) developed a similar chart that relates the dimensionless
 571 friction factor to Reynold's number for porous media in all possible flow regimes (Holdich,
 572 2002). This friction factor can be used to evaluate the medium resistance to flow, or in other
 573 words, it can be used to estimate the pressure needed to pass flow at a specific rate through the
 574 porous medium within any flow regime (Hlushkou & Tallarek, 2006).

575 The friction factor (f) in porous media can be determined by neglecting the small difference
 576 between K_D and K_F , then Equation 2 can be rewritten as $f = \frac{1}{F_o} + 1$, where $f = \frac{\Delta P}{L\beta\rho v^2}$ and $F_o =$
 577 $\frac{K_D\beta\rho v}{\mu}$ (Macdonald et al., 1979; Macedo et al., 2001; Pamuk & Özdemir, 2012). Fig. 12 shows
 578 that the friction between the medium particles and the fluid decreases with increasing the
 579 Forchheimer number, i.e. when the fluid velocity increases. Friction factor and Forchheimer
 580 number predictions for all samples are in excellent agreement with each other and in agreement
 581 with the experimentally measured values. This agreement is because all the parameters (f , K_D
 582 and β) used to develop the figure are predicted from Forchheimer equation. However, this is
 583 not the case when the friction factor is plotted versus Reynold's number (not presented), and
 584 this shows that Forchheimer number is a better dimensionless parameter that can be used to
 585 describe flow through porous media. The resulting friction factor versus Forchheimer number
 586 curve is a unique relationship that agrees very well to the results presented by Geertsma (1974)
 587 and can be used for all samples regardless of its degree of heterogeneity.



588
 589 **Fig. 12** The medium friction factor (f) versus Forchheimer number (F_o).

590 **3.7. Tortuosity**

591 Wang et al. (1999) defined tortuosity in isotropic media as

$$\tau = \frac{\hat{L}}{\tilde{L}_e} \quad (16)$$

592 where \hat{L} is the average streamwise flow path or the actual distance including any encountered
 593 curves between two points and \tilde{L}_e is the straight distance between these two points. Other
 594 authors define tortuosity as the square of this ratio (Dullien, 1992). Thauvin and Mohanty
 595 (1998) and Wang et al. (1999) investigated the effect of tortuosity on the non-Darcy coefficient
 596 and concluded that its effect is negligible. As it is difficult to obtain tortuosity either
 597 experimentally or numerically, Muljadi et al. (2015) used the method proposed by Duda et al.
 598 (2011) and Koponen et al. (1996) to obtain tortuosity from the fluid velocity field without the
 599 need to determine flow paths as follows:

$$\tau = \frac{\langle |v_{inters}| \rangle}{\langle v_x \rangle} \geq 1 \quad (17)$$

600 where $\langle |v_{inters}| \rangle$ is the average magnitude of interstitial velocity over the entire volume and
 601 $\langle v_x \rangle$ is the volumetric average of its component along the macroscopic flow direction.

602 In the proposed PN model, the discharge through each pore throat can be easily determined
 603 after solving the pressure value at each node, then the velocity of flow in each pore throat can
 604 be determined by dividing the discharge value in each pore throat by the cross-sectional area
 605 of that throat. The velocity through the connected pore bodies can be determined by dividing
 606 the pore throat discharge by the cross-sectional area of the pore body as well. Then the overall
 607 average fluid velocity ($v_{i-j,tot}$) through the pore throat and the two connected pore bodies can
 608 be estimated as the length harmonic average of the velocities (Equation 18, Fig. 1).

$$\frac{L_{i-j,tot}}{v_{i-j,tot}} = \frac{L_i}{v_i} + \frac{L_{i-j}}{v_{i-j}} + \frac{L_j}{v_j} \quad (18)$$

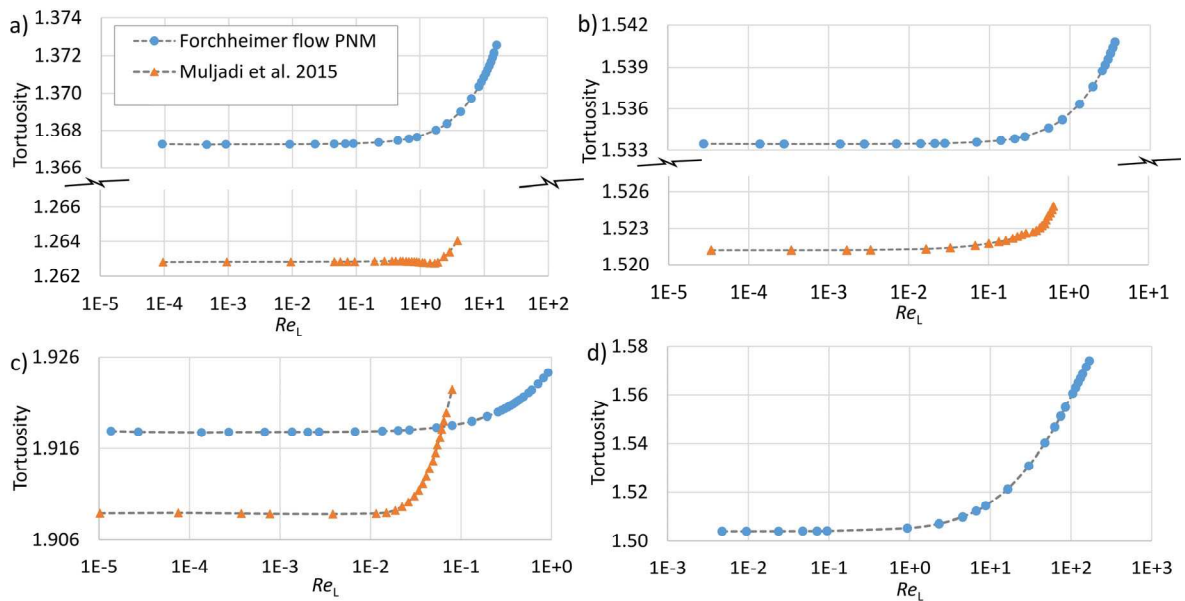
609 where v_{i-j} is the velocity of flow through the pore throat that connects the two pore bodies i
 610 and j , v_i and v_j are the fluid velocity through the pore bodies i and j .

611 Finally, the volumetric average interstitial velocity $\langle |v_{inters}| \rangle$ can be obtained as

$$\langle |v_{inters}| \rangle = \frac{\sum (v_{i-j,tot} a_{i-j})}{\sum a_{i-j}} \quad (19)$$

612 Similarly, v_x for each pore throat can be estimated as the X -component, along the macroscopic
 613 flow direction, corresponding to each $v_{i-j,tot}$. Then, $\langle v_x \rangle$ can be obtained by replacing

614 $v_{i-j,tot}$ by v_x in Equation 19. Fig. 13 shows that tortuosity increases slightly with increasing
 615 the Reynold's number, this is due to the increase in velocities and the possible occurrence of
 616 some eddies. All samples in Fig. 13 have a trend similar to that obtained by Muljadi et al.
 617 (2015) and Chukwudozie et al. (2012) and are in agreement (varying with in less than 8%) with
 618 the values obtained by Muljadi et al. (2015). It is noticeable that in Fig. 13c, the increasing
 619 trend of τ is delayed compared to Muljadi et al. (2015), this is attributed to some discrepancies
 620 in predicting the flow velocities and pressures loss (as in Fig. 6c) for Estailades. Due to the
 621 heterogeneity of Estailades, its tortuosity is larger than other samples. This is due to the poor
 622 connectivity between different zones in the sample, as in Section 3.5., so each fluid particle
 623 may need to travel a longer path.



624
625

626 **Fig. 13** Tortuosity versus Re_L for; a) Beadpack, b) is Bentheimer, c) Estailades and d) Packed
 627 sphere samples.

628 4. Conclusion

629 In this work, Darcy permeability, apparent permeability, non-Darcy coefficient and tortuosity
 630 were estimated for four porous samples (beadpack, Bentheimer sandstone, Estailades
 631 carbonate and packed spheres) with different degrees of heterogeneity using pore-network
 632 modelling and applying the Forchheimer equation. The proposed model overcomes most of the
 633 limitations in previous studies that used pore-network modelling to simulate non-Darcy flow;
 634 limited coordination number, 2D simulations only, inaccuracy of some equations, limitation

635 regarding the use of regular structured networks only and lack of calibration. In addition, the
636 onset of non-Darcy flow was fully investigated in detail for all samples.

637 Based on findings of this research, it is concluded that Forchheimer number (F_o), instead of the
638 permeability-based Reynold's number (Re_K) or standard Reynold's number (Re_L), can be used
639 as a criterion to determine the onset of non-Darcy flow. This is because Forchheimer number
640 accounts for Darcy permeability, the Forchheimer coefficient and the medium degree of
641 heterogeneity. The onset of non-Darcy flow, determined at $K^*=0.99$ and using Re_K , is highly
642 dependent on the degree of heterogeneity. For Bentheimer sandstone the onset of non-Darcy
643 flow is one order of magnitude smaller than in the case of beadpack, and for Estailades the
644 onset of non-Darcy flow is three orders of magnitudes smaller than in the case of beadpack.
645 Nevertheless, the Forchheimer number values for the onset of non-Darcy flow for the four
646 samples ranged from 0.01 to 0.1 and this is in agreement with Andrade et al. (1999).

647 The Darcy Permeabilities (K_D) and Forchheimer coefficients (β) for all samples are in a good
648 agreement (varying within 15.2% and 54% respectively) with the values obtained either in the
649 laboratory or by Muljadi et al. (2015) for the same samples, except in the case of Bentheimer,
650 its β value varied 126%.

651 The medium friction factor is a good feature that can be used to calculate the pressure gradient
652 at different velocities for different flow regimes, regardless the heterogeneity of the medium,
653 if the Darcy permeability and Forchheimer coefficient are known. It was found that the medium
654 friction coefficient decreases when the fluid velocity increases. Following the Forchheimer
655 equation, the medium friction factor versus Forchheimer number curve is identical for all media
656 regardless of their degree of heterogeneity. Tortuosity was found to increase slightly with
657 increasing the flow velocity, in all samples.

658 For highly heterogeneous media, i.e. Estailades, the pressure variation between pores at one
659 cross-section (perpendicular to the flow direction) may extend up to 98% of the overall pressure
660 drop. This is mainly caused by the medium heterogeneity that creates some stagnant zones with
661 low pressure values next to other zones with high pressure values.

662 The pore-network modelling approach has been shown to be computationally more efficient in
663 comparison with direct flow simulations and could dramatically reduce the running time from
664 few hours (3 hours and 37 minutes for the Estailades model in Muljadi et al. (2015) work)
665 using 16 parallel computer nodes to less than one minute using a standard PC, but it is still
666 relatively memory demanding when a large number of pore bodies is used, especially for non-

667 linear flow simulations. For instance, a pore-network with 120,000 pore bodies requires 185
668 GB Ram. Nevertheless, in terms of pore geometries, direct numerical simulation is believed to
669 be more accurate than pore-network modelling which simplifies the irregular pore shapes into
670 pores with simple geometries for which the analytical flow equations can be applied.

671 **Acknowledgment**

672 We acknowledge the fund given to the first author from the Newton-Mosharafa program as a
673 collaboration between the British Council and the Egyptian Ministry of Higher Education. Dr
674 Bagus Muljadi and Dr Ali Raeini are acknowledged for providing part of the CT-images used
675 in this study. The anonymous reviewers are acknowledged for their constructive comments.

676 **References**

- 677 Abdelall, F. F., Hahn, G., Ghiaasiaan, S. M., Abdel-Khalik, S. I., Jeter, S. S., Yoda, M., & Sadowski, D. L.
678 (2005). Pressure drop caused by abrupt flow area changes in small channels. *Experimental*
679 *Thermal and Fluid Science*, 29(4), 425-434.
680 doi:<https://doi.org/10.1016/j.expthermflusci.2004.05.001>
- 681 Akhlaghi Amiri, H. A., & Hamouda, A. A. (2013). Evaluation of level set and phase field methods in
682 modeling two phase flow with viscosity contrast through dual-permeability porous medium.
683 *International Journal of Multiphase Flow*, 52, 22-34.
684 doi:<http://dx.doi.org/10.1016/j.ijmultiphaseflow.2012.12.006>
- 685 Al-Raoush, R., Thompson, K., & Willson, C. S. (2003). Comparison of Network Generation Techniques
686 for Unconsolidated Porous Media. *Soil Science Society of America Journal*, 67(6), 1687-1700.
687 doi:10.2136/sssaj2003.1687
- 688 Alfonsi, G. (2011). On Direct Numerical Simulation of Turbulent Flows. *Applied Mechanics Reviews*,
689 64(2), 020802-020802-020833. doi:10.1115/1.4005282
- 690 Aly, A. M., & Asai, M. (2015). Modelling of Non-Darcy Flows through Porous Media Using Extended
691 Incompressible Smoothed Particle Hydrodynamics. *Numerical Heat Transfer, Part B:*
692 *Fundamentals*, 67(3), 255-279. doi:10.1080/10407790.2014.955772
- 693 Andrade, J. S., Costa, U. M. S., Almeida, M. P., Makse, H. A., & Stanley, H. E. (1999). Inertial Effects on
694 Fluid Flow through Disordered Porous Media. *Physical Review Letters*, 82(26), 5249-5252.
695 doi:10.1103/PhysRevLett.82.5249
- 696 Aziz, R., Joekar-Niasar, V., & Martinez-Ferrer, P. (2018). Pore-scale insights into transport and mixing
697 in steady-state two-phase flow in porous media. *International Journal of Multiphase Flow*,
698 109, 51-62. doi:<https://doi.org/10.1016/j.ijmultiphaseflow.2018.07.006>
- 699 Babaei, M., & Joekar-Niasar, V. (2016). A transport phase diagram for pore-level correlated porous
700 media. *Advances in Water Resources*, 92, 23-29.
701 doi:<http://dx.doi.org/10.1016/j.advwatres.2016.03.014>
- 702 Balhoff, M. T., & Wheeler, M. F. (2009). A Predictive Pore-Scale Model for Non-Darcy Flow in Porous
703 Media. *SPE Journal*, 14(03), 579-587.
- 704 Bandara, U. C., Tartakovsky, A. M., Oostrom, M., Palmer, B. J., Grate, J., & Zhang, C. (2013).
705 Smoothed particle hydrodynamics pore-scale simulations of unstable immiscible flow in
706 porous media. *Advances in Water Resources*, 62, Part C, 356-369.
707 doi:<http://dx.doi.org/10.1016/j.advwatres.2013.09.014>
- 708 Bear, J. (1972). *Dynamics of Fluids in Porous Media*. Elsevier, New York.
- 709 Belhaj, H. A., Agha, K. R., Nouri, A. M., Butt, S. D., Vaziri, H. H., & Islam, M. R. (2003). *Numerical*
710 *Modeling of Forchheimer's Equation to Describe Darcy and Non-Darcy Flow in Porous Media*.

711 Paper presented at the SPE Asia Pacific Oil and Gas Conference and Exhibition, Jakarta,
712 Indonesia. <https://doi.org/10.2118/80440-MS>

713 Bijeljic, B., & Blunt, M. J. (2007). Pore-scale modeling of transverse dispersion in porous media.
714 *Water Resources Research*, 43(12), W12S11. doi:10.1029/2006WR005700

715 Bijeljic, B., Mostaghimi, P., & Blunt, M. J. (2013a). Insights into non-Fickian solute transport in
716 carbonates. *Water Resources Research*, 49(5), 2714-2728. doi:10.1002/wrcr.20238

717 Bijeljic, B., Muggeridge, A. H., & Blunt, M. J. (2004). Pore-scale modeling of longitudinal dispersion.
718 *Water Resources Research*, 40(11), W11501. doi:10.1029/2004WR003567

719 Bijeljic, B., Raeini, A., Mostaghimi, P., & Blunt, M. J. (2013b). Predictions of non-Fickian solute
720 transport in different classes of porous media using direct simulation on pore-scale images.
721 *Physical Review E*, 87(1), 013011.

722 Bird, R. B., Stewart, W. E., & Lightfoot, E. N. (1960). *Transport phenomena*. New York: John Wiley and
723 Sons.

724 Bird, R. B., Stewart, W. E., & Lightfoot, E. N. (1961). *Transport phenomena*, John Wiley and Sons, Inc.,
725 New York (1960). 780 pages. \$11.50. *AIChE Journal*, 7(2), 5J-6J. doi:10.1002/aic.690070245

726 Blunt, M. J., Bijeljic, B., Dong, H., Gharbi, O., Iglauer, S., Mostaghimi, P., Paluszny, A., & Pentland, C.
727 (2013). Pore-scale imaging and modelling. *Advances in Water Resources*, 51, 197-216.
728 doi:<http://dx.doi.org/10.1016/j.advwatres.2012.03.003>

729 Bryant, S., & Blunt, M. (1992). Prediction of relative permeability in simple porous media. *Physical*
730 *Review A*, 46(4), 2004-2011.

731 Bryant, S. L., Mellor, D. W., & Cade, C. A. (1993). Physically representative network models of
732 transport in porous media. *AIChE Journal*, 39(3), 387-396. doi:10.1002/aic.690390303

733 Carman, P. C. (1937). Fluid flow through granular beds. *Chemical Engineering Research and Design*,
734 75, S32-S48. doi:[https://doi.org/10.1016/S0263-8762\(97\)80003-2](https://doi.org/10.1016/S0263-8762(97)80003-2)

735 Celia, M. A., Reeves, P. C., & Ferrand, L. A. (1995). Recent advances in pore scale models for
736 multiphase flow in porous media. *Reviews of Geophysics*, 33(S2), 1049-1057.
737 doi:10.1029/95RG00248

738 Çengel, Y. A., & Cimbala, J. M. (2006). *Fluid mechanics: Fundamentals and applications*. Boston:
739 McGraw-Hill Higher Education.

740 Chukwudozie, C. P., Tyagi, M., Sears, S. O., & White, C. D. (2012). Prediction of Non-Darcy
741 Coefficients for Inertial Flows Through the Castlegate Sandstone Using Image-Based
742 Modeling. *Transport in Porous Media*, 95(3), 563-580. doi:10.1007/s11242-012-0062-5

743 Comiti, J., Sabiri, N. E., & Montillet, A. (2000). Experimental characterization of flow regimes in
744 various porous media — III: limit of Darcy's or creeping flow regime for Newtonian and
745 purely viscous non-Newtonian fluids. *Chemical Engineering Science*, 55(15), 3057-3061.
746 doi:[http://dx.doi.org/10.1016/S0009-2509\(99\)00556-4](http://dx.doi.org/10.1016/S0009-2509(99)00556-4)

747 Crane. (1942). *Flow of fluids through valves, fittings and pipe*. Chicago, Ill: Crane co.

748 Darcy, H. (1856). Les Fontaines Publiques de la Vile de Dijon. *Victor Dalmond, Paris*.

749 Duda, A., Koza, Z., & Matyka, M. (2011). Hydraulic tortuosity in arbitrary porous media flow. *Physical*
750 *Review E*, 84(3), 036319.

751 Dullien, F. A. L. (1992). *Porous Media: Fluid Transport and Pore Structure*. San Diego: Academic Press.

752 Durlofsky, L., & Brady, J. F. (1987). Analysis of the Brinkman equation as a model for flow in porous
753 media. *The Physics of Fluids*, 30(11), 3329-3341. doi:10.1063/1.866465

754 El-Zehairy, A. A., Lubczynski, M. W., & Gurwin, J. (2018). Interactions of artificial lakes with
755 groundwater applying an integrated MODFLOW solution. *Hydrogeology Journal*, 26(1), 109-
756 132. doi:10.1007/s10040-017-1641-x

757 Ergun, S. (1952). Fluid Flow through Packed Columns. *Chem. Eng. Prog.*, 48, 89-94.

758 Finney, J. L. (1970). Random packings and the structure of simple liquids. I. The geometry of random
759 close packing. *Proceedings of the Royal Society of London. A. Mathematical and Physical*
760 *Sciences*, 319(1539), 479-493. doi:doi:10.1098/rspa.1970.0189

761 Forchheimer, P. (1901). Wasserbewegung durch Boden. *Zeitschrift des Vereins deutscher Ingenieure*
762 *45, no. 1: 1782–1788.*

763 Gao, S., Meegoda, J. N., & Hu, L. (2012). Two methods for pore network of porous media.
764 *International Journal for Numerical and Analytical Methods in Geomechanics, 36(18), 1954-*
765 *1970. doi:10.1002/nag.1134*

766 Geertsma, J. (1974). Estimating the Coefficient of Inertial Resistance in Fluid Flow Through Porous
767 Media. *Society of Petroleum Engineers Journal, 14(05), 445-450. doi:10.2118/4706-PA*

768 Geiger, G. E. (1964). *Sudden contraction losses in single and two-phase flow.* (Ph.D. thesis),
769 University of Pittsburgh, Pittsburgh, PA.

770 Guadagnini, A., Blunt, M. J., Riva, M., & Bijeljic, B. (2014). Statistical Scaling of Geometric
771 Characteristics in Millimeter Scale Natural Porous Media. *Transport in Porous Media, 101(3),*
772 *465-475. doi:10.1007/s11242-013-0254-7*

773 Guo, H., Wang, L., Yu, J., Ye, F., Ma, C., & Li, Z. (2010). Local resistance of fluid flow across sudden
774 contraction in small channels. *Frontiers of Energy and Power Engineering in China, 4(2), 149-*
775 *154. doi:10.1007/s11708-009-0060-7*

776 Hagen, G. (1839). Ueber die Bewegung des Wassers in engen cylindrischen Röhren. *Annalen der*
777 *Physik, 122(3), 423-442. doi:10.1002/andp.18391220304*

778 Hlushkou, D., & Tallarek, U. (2006). Transition from creeping via viscous-inertial to turbulent flow in
779 fixed beds. *Journal of Chromatography A, 1126(1–2), 70-85.*
780 doi:<https://doi.org/10.1016/j.chroma.2006.06.011>

781 Holdich, R. G. (2002). *Fundamentals of particle technology.* Midland Information Technology and
782 Publishing, Shepshed.

783 HSL. (2013). A collection of Fortran codes for large scale scientific computation.
784 <http://www.hsl.rl.ac.uk>.

785 Janicek, J., & Katz, D. (1955). Applications of unsteady state gas flow calculations. *In: Proceedings of*
786 *University of Michigan research conference.*

787 Joekar-Niasar, V., & Hassanizadeh, S. M. (2012). Analysis of Fundamentals of Two-Phase Flow in
788 Porous Media Using Dynamic Pore-Network Models: A Review. *Critical Reviews in*
789 *Environmental Science and Technology, 42(18), 1895-1976.*
790 doi:10.1080/10643389.2011.574101

791 Joekar-Niasar, V., Prodanović, M., Wildenschild, D., & Hassanizadeh, S. M. (2010). Network model
792 investigation of interfacial area, capillary pressure and saturation relationships in granular
793 porous media. *Water Resources Research, 46(6), W06526. doi:10.1029/2009WR008585*

794 Joekar Niasar, V., Hassanizadeh, S. M., Pyrak-Nolte, L. J., & Berentsen, C. (2009). Simulating drainage
795 and imbibition experiments in a high-porosity micromodel using an unstructured pore
796 network model. *Water Resources Research, 45(2), W02430. doi:10.1029/2007WR006641*

797 Kays, W. M. (1950). Loss Coefficient for Abrupt Changes in Flow Cross Section with Reynolds Number
798 Flow in Single and Multiple Tube Systems. *Transactions of the American Society of*
799 *Mechanical Engineers, 72, 1067-1074.*

800 Knackstedt, M. A., Sheppard, A. P., & Sahimi, M. (2001). Pore network modelling of two-phase flow
801 in porous rock: the effect of correlated heterogeneity. *Advances in Water Resources, 24(3–*
802 *4), 257-277. doi:http://dx.doi.org/10.1016/S0309-1708(00)00057-9*

803 Koponen, A., Kataja, M., & Timonen, J. (1996). Tortuous flow in porous media. *Physical Review E,*
804 *54(1), 406-410.*

805 Kozeny, J. (1927). Über kapillare Leitung des Wassers im Boden. *Akad. Wiss. Wien, 136, 271-306.*
806 doi:citeulike-article-id:4155258

807 Kuwata, Y., & Suga, K. (2015). Large eddy simulations of pore-scale turbulent flows in porous media
808 by the lattice Boltzmann method. *International Journal of Heat and Fluid Flow, 55, 143-157.*
809 doi:<http://dx.doi.org/10.1016/j.ijheatfluidflow.2015.05.015>

810 Lao, H. W., Neeman, H. J., & Papavassiliou, D. V. (2004). A pore network model for the calculation of
811 non-Darcy flow coefficients in fluid flow through porous media. *Chemical Engineering*
812 *Communications*, 191(10), 1285-1322. doi:10.1080/00986440490464200

813 Lemley, E. C., Papavassiliou, D. V., & Neeman, H. J. (2007). *Non-Darcy Flow Pore Network Simulation:*
814 *Development and Validation of a 3D Model*. Paper presented at the ASME/JSME 2007 5th
815 Joint Fluids Engineering Conference.

816 Liu, X., Civan, F., & Evans, R. D. (1995). Correlation of the Non-Darcy Flow Coefficient. *Journal of*
817 *Canadian Petroleum Technology*, 34(10), 6. doi:10.2118/95-10-05

818 Macdonald, I. F., El-Sayed, M. S., Mow, K., & Dullien, F. A. L. (1979). Flow through Porous Media-the
819 Ergun Equation Revisited. *Industrial & Engineering Chemistry Fundamentals*, 18(3), 199-208.
820 doi:10.1021/i160071a001

821 Macedo, H. H., Costa, U. M. S., & Almeida, M. P. (2001). Turbulent effects on fluid flow through
822 disordered porous media. *Physica A: Statistical Mechanics and its Applications*, 299(3-4),
823 371-377. doi:[http://dx.doi.org/10.1016/S0378-4371\(01\)00257-6](http://dx.doi.org/10.1016/S0378-4371(01)00257-6)

824 Mason, G., & Morrow, N. R. (1991). Capillary behavior of a perfectly wetting liquid in irregular
825 triangular tubes. *Journal of Colloid and Interface Science*, 141(1), 262-274.
826 doi:[http://dx.doi.org/10.1016/0021-9797\(91\)90321-X](http://dx.doi.org/10.1016/0021-9797(91)90321-X)

827 Moin, P., & Mahesh, K. (1998). DIRECT NUMERICAL SIMULATION: A Tool in Turbulence Research.
828 *Annual Review of Fluid Mechanics*, 30(1), 539-578. doi:10.1146/annurev.fluid.30.1.539

829 Momen, A. M., Sherif, S. A., & Lear, W. (2016). An Analytical-Numerical Model for Two-Phase Slug
830 Flow through a Sudden Area Change in Microchannels. *Journal of Applied Fluid Mechanics*,
831 *Vol. 9, No. 4, pp. 1839-1850*.

832 Moody, L. F. (1944). Friction Factors for Pipe Flow. *Transactions of the American Society of*
833 *Mechanical Engineers*, 66, 671-681.

834 Mostaghimi, P., Bijeljic, B., & Blunt, M. (2012). Simulation of Flow and Dispersion on Pore-Space
835 Images. doi:10.2118/135261-PA

836 Mousavi Nezhad, M., & Javadi, A. A. (2011). Stochastic Finite-Element Approach to Quantify and
837 Reduce Uncertainty in Pollutant Transport Modeling. *Journal of Hazardous, Toxic, and*
838 *Radioactive Waste*, 15(3), 208-215. doi:doi:10.1061/(ASCE)HZ.1944-8376.0000055

839 Mousavi Nezhad, M., Javadi, A. A., & Rezaia, M. (2011). Modeling of contaminant transport in soils
840 considering the effects of micro- and macro-heterogeneity. *Journal of Hydrology*, 404(3),
841 332-338. doi:<https://doi.org/10.1016/j.jhydrol.2011.05.004>

842 Muljadi, B. P., Blunt, M. J., Raeini, A. Q., & Bijeljic, B. (2015). The impact of porous media
843 heterogeneity on non-Darcy flow behaviour from pore-scale simulation. *Advances in Water*
844 *Resources*. doi:<http://dx.doi.org/10.1016/j.advwatres.2015.05.019>

845 Oostrom, M., Mehmani, Y., Romero-Gomez, P., Tang, Y., Liu, H., Yoon, H., Kang, Q., Joekar-Niasar, V.,
846 Balhoff, M. T., Dewers, T., Tartakovsky, G. D., Leist, E. A., Hess, N. J., Perkins, W. A.,
847 Rakowski, C. L., Richmond, M. C., Serkowski, J. A., Werth, C. J., Valocchi, A. J., Wietsma, T.
848 W., & Zhang, C. (2016). Pore-scale and continuum simulations of solute transport
849 micromodel benchmark experiments. *Computational Geosciences*, 20(4), 857-879.
850 doi:10.1007/s10596-014-9424-0

851 Oren, P. E., Bakke, S., & Arntzen, O. J. (1998). Extending Predictive Capabilities to Network Models.
852 doi:10.2118/52052-PA

853 Pamuk, M. T., & Özdemir, M. (2012). Friction factor, permeability and inertial coefficient of
854 oscillating flow through porous media of packed balls. *Experimental Thermal and Fluid*
855 *Science*, 38, 134-139. doi:<http://dx.doi.org/10.1016/j.expthermflusci.2011.12.002>

856 Patzek, T. W., & Silin, D. B. (2001). Shape Factor and Hydraulic Conductance in Noncircular
857 Capillaries. *Journal of Colloid and Interface Science*, 236(2), 295-304.
858 doi:<http://dx.doi.org/10.1006/jcis.2000.7413>

859 Poinso, T., Candel, S., & Trouvé, A. (1995). Applications of direct numerical simulation to premixed
860 turbulent combustion. *Progress in Energy and Combustion Science*, 21(6), 531-576.
861 doi:[https://doi.org/10.1016/0360-1285\(95\)00011-9](https://doi.org/10.1016/0360-1285(95)00011-9)

862 Poiseuille, J. L. M. (1841). Recherches expérimentales sur le mouvement des liquides dans les tubes
863 de très petits diamètres. *Memoires Presentes par Divers Savants a l'Academie Royal de l'*
864 *Institut de France*,9: 433-544.

865 Prodanović, M., & Bryant, S. L. (2006). A level set method for determining critical curvatures for
866 drainage and imbibition. *Journal of Colloid and Interface Science*, 304(2), 442-458.
867 doi:<http://dx.doi.org/10.1016/j.jcis.2006.08.048>

868 Raeini, A. Q., Bijeljic, B., & Blunt, M. J. (2017). Generalized network modeling: Network extraction as
869 a coarse-scale discretization of the void space of porous media. *Physical Review E*, 96(1),
870 013312. doi:10.1103/PhysRevE.96.013312

871 Raeini, A. Q., Bijeljic, B., & Blunt, M. J. (2018). Generalized network modeling of capillary-dominated
872 two-phase flow. *Physical Review E*, 97(2), 023308. doi:10.1103/PhysRevE.97.023308

873 Raeini, A. Q., Blunt, M. J., & Bijeljic, B. (2012). Modelling two-phase flow in porous media at the pore
874 scale using the volume-of-fluid method. *Journal of Computational Physics*, 231(17), 5653-
875 5668. doi:<https://doi.org/10.1016/j.jcp.2012.04.011>

876 Ruth, D., & Ma, H. (1992). On the derivation of the Forchheimer equation by means of the averaging
877 theorem. *Transport in Porous Media*, 7(3), 255-264. doi:10.1007/bf01063962

878 Ruth, D. W., & Ma, H. (1993). Numerical analysis of viscous, incompressible flow in a diverging-
879 converging RUC. *Transport in Porous Media*, 13(2), 161-177. doi:10.1007/bf00654408

880 Sahimi, M. (2011). Continuum versus Discrete Models. *In Flow and Transport in Porous Media and*
881 *Fractured Rock*.

882 Tartakovsky, A. M., Trask, N., Pan, K., Jones, B., Pan, W., & Williams, J. R. (2015). Smoothed particle
883 hydrodynamics and its applications for multiphase flow and reactive transport in porous
884 media. *Computational Geosciences*, 1-28. doi:10.1007/s10596-015-9468-9

885 Thauvin, F., & Mohanty, K. K. (1998). Network Modeling of Non-Darcy Flow Through Porous Media.
886 *Transport in Porous Media*, 31(1), 19-37. doi:10.1023/a:1006558926606

887 Vafai, K., & Tien, C. L. (1981). Boundary and inertia effects on flow and heat transfer in porous
888 media. *International Journal of Heat and Mass Transfer*, 24(2), 195-203.
889 doi:[http://dx.doi.org/10.1016/0017-9310\(81\)90027-2](http://dx.doi.org/10.1016/0017-9310(81)90027-2)

890 Valvatne, P. H., & Blunt, M. J. (2004). Predictive pore-scale modeling of two-phase flow in mixed wet
891 media. *Water Resources Research*, 40(7), W07406. doi:10.1029/2003WR002627

892 Wang, X., Thauvin, F., & Mohanty, K. K. (1999). Non-Darcy flow through anisotropic porous media.
893 *Chemical Engineering Science*, 54(12), 1859-1869. doi:[http://dx.doi.org/10.1016/S0009-2509\(99\)00018-4](http://dx.doi.org/10.1016/S0009-2509(99)00018-4)

894

895 Wilkinson, D. (1984). Percolation model of immiscible displacement in the presence of buoyancy
896 forces. *Physical Review A*, 30(1), 520-531.

897 Wu, J., Hu, D., Li, W., & Cai, X. I. N. (2016). A review on non-Darcy flow-Forchheimer equation,
898 Hydraulic radius model, fractal model and experiment. *Fractals*, 24(02), 1630001.
899 doi:10.1142/S0218348X16300014

900 Xiong, Q., Baychev, T. G., & Jivkov, A. P. (2016). Review of pore network modelling of porous media:
901 Experimental characterisations, network constructions and applications to reactive
902 transport. *Journal of Contaminant Hydrology*, 192, 101-117.
903 doi:<http://dx.doi.org/10.1016/j.jconhyd.2016.07.002>

904 Zeng, Z., & Grigg, R. (2006). A Criterion for Non-Darcy Flow in Porous Media. *Transport in Porous*
905 *Media*, 63(1), 57-69. doi:10.1007/s11242-005-2720-3

906 Zhang, J., & Xing, H. (2012). Numerical modeling of non-Darcy flow in near-well region of a
907 geothermal reservoir. *Geothermics*, 42, 78-86.
908 doi:<https://doi.org/10.1016/j.geothermics.2011.11.002>

909 Zimmerman, R. W., Al-Yaarubi, A., Pain, C. C., & Grattoni, C. A. (2004). Non-linear regimes of fluid
910 flow in rock fractures. *International Journal of Rock Mechanics and Mining Sciences*, 41, 163-
911 169. doi:<https://doi.org/10.1016/j.ijrmms.2004.03.036>
912
913